Journal of Crystal Growth 112 (1991) 244–282
North-Holland

Review paper

Stability and shapes of cellular profiles in directional solidification: expansion and matching methods

John D. WEEKS *, Wim van Saarloos **
AT&T Bell Laboratories, Murray Hill, New Jersey 07974, USA

and

Martin Grant
Department of Physics, McGill University, Montreal, Quebec, Canada H3A 2T8

Received 15 October 1990

Ideas based on constitutional supercooling suggest that the periodic steady state cellular patterns seen in the directional solidification of systems with small partition coefficient may be unstable if the impurity concentration in the melt just in front of the tips falls into the two phase (miscibility gap) region of the phase diagram. This gives a simple stability criterion relating the position of the tips of the cells to the pulling velocity that is in good qualitative agreement with the limited experimental data available in the cellular regime. Implications of this criterion for a particular class of steady state solutions derived using asymptotic matching methods are explored. These solutions arise from a generalization to finite Péclet number for systems with small partition coefficient of the ideas of Dombre and Hakim relating directional solidification patterns to viscous (Saffman–Taylor) fingers. Families of steady state solutions yielding both small amplitude interface patterns as well as fingerlike solutions with narrow deep grooves are accurately described by the methods discussed herein. A systematic expansion method provides corrections to the classical Scheil shapes for the grooves. However, the stability criterion, as well as other considerations, suggest that the entire class of narrow grooved solutions found by the matching methods may be unstable. Comparison with other numerical work suggests that other branches of narrow grooved solutions exist and are relevant to experiments. Several experimental and numerical tests of these ideas are proposed.

1. Introduction

A variety of interesting patterns can form during the directional solidification of a binary mixture [1–3]. In this technologically important process, solidification occurs when a thin sample of melt is pulled through a fixed temperature gradient. As the pulling speed V is increased, the initial planar solid–liquid interface becomes unstable. While the detailed behavior very near threshold is quite complex (and difficult to study experimentally), at somewhat larger pulling speeds typically one encounters finite amplitude steady state patterns like that shown in fig. 1a, or fingerlike cells with deep grooves as in fig. 1b. These figures are taken from theoretical work by Ungar and Brown [4], but experimental examples of both kinds of patterns have been observed by Trivedi [5] in the succinonitrile–acetone system and, more recently, by de Cheveigné and coworkers [6] in the CBr_4–Br_2 system. An example of cells with grooves observed in experiments of Cladis et al. [7] is shown in fig. 2.

A convenient way to display the experimental results is to plot the wavelength λ of cellular

* Present address: Institute for Physical Science and Technology, University of Maryland, College Park, Maryland 20742, USA.
** Present address: Instituut Lorentz. University of Leiden, Nieuwsteeg 18, 2311 SB Leiden, Netherlands.

0022-0248/91/$03.50

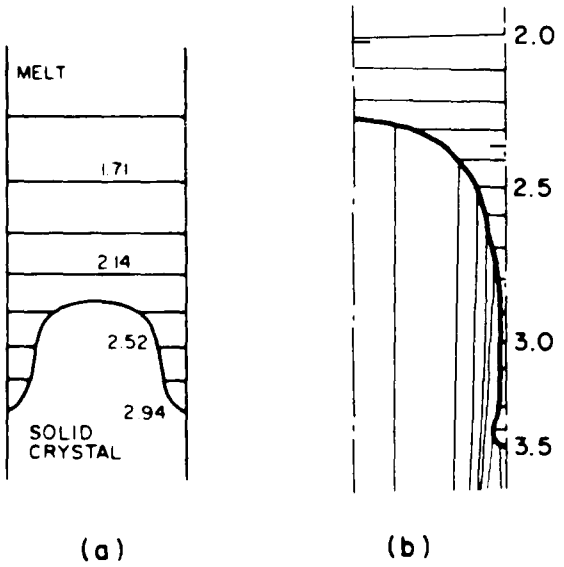

Fig. 1. Examples of the cell profiles calculated numerically by Ungar and Brown [4,73]. The thin solid lines show the iso-concentration lines. (a) A finite amplitude cell at Péclet number $p = \lambda V/2D = 0.4$, $\nu \approx 1.2$, $\sigma \approx 0.026$. (b) Half of a cell with a groove at Péclet number $p = \lambda V/2D = 0.4$, $\nu = 1.33$ and $\sigma = 0.016$. The parameter σ is defined in eq. (9.1).

patterns versus the pulling velocity V, and compare this scale to the length scales associated with a linear stability analysis of the planar interface. Such a plot is reproduced in fig. 3 from the work of de Cheveigné et al. [8]. In this figure, the wavelength of perturbations about the planar interface that are neutrally stable (i.e. neither grow nor decay) is indicated by a solid line. (Note that the neutrally stable modes represent valid steady state solutions of infinitesimal amplitude). Curves for two different temperature gradients are shown. The minimum threshold velocity V_c at which the planar interface first goes unstable is denoted by the square symbol at the bottom of the curves. Perturbations about the planar interface with wavelengths in the wide band between these two solid lines are linearly unstable; we therefore refer to this region as the planar instability band. The selected cells for a given pulling velocity in the experiments of de Cheveigné et al. [8] have wavelengths that lie within the planar instability band in the narrow dashed region whose wavelength is a factor 3–5 larger than the smallest neutral stability value. This is what is typically observed [9].

Most theoretical studies of these patterns have concentrated on a steady state analysis. Recent work, both numerical and analytic, has established that the steady state equations describing directional solidification (DS) admit a *continuous family* of periodic solutions of varying wavelengths for a given set of experimental conditions. Dombre and Hakim [10] carried out a particularly elegant analytic demonstration of this fact for a simplified model of DS with a partition coefficient of unity in the limit that the Péclet number p tended towards zero. (The Péclet number p compares the scale of the pattern to the range of the diffusion

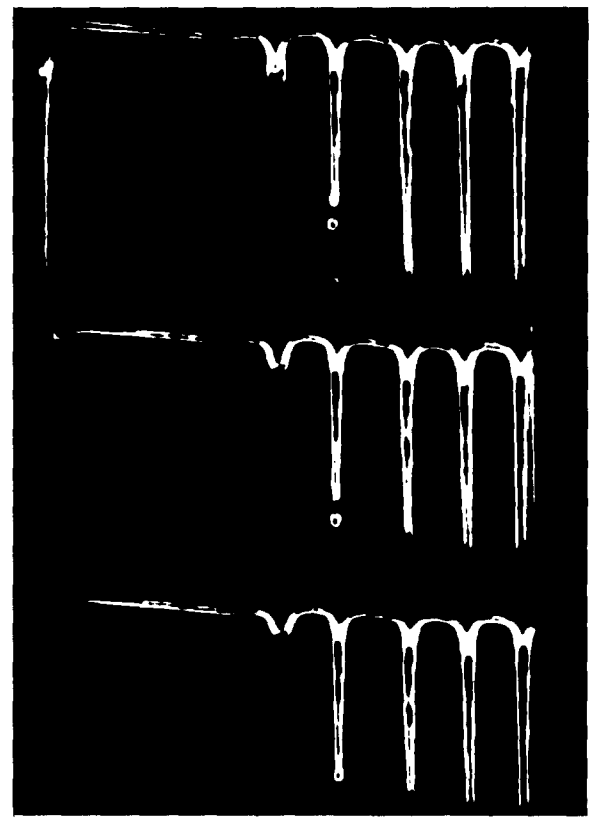

Fig. 2. Example of some experimental cell patterns at three different moments in time, showing the periodic release of bubbles from the bottom of a groove. The initial profile is the one on the bottom, and these pictures were taken while the cellular region was expanding into the planar region on the left. In this photo, the spatial variation of the contrast has been enhanced using computer image processing, so that the interfaces show up as white lines (photo courtesy of P.E. Cladis).

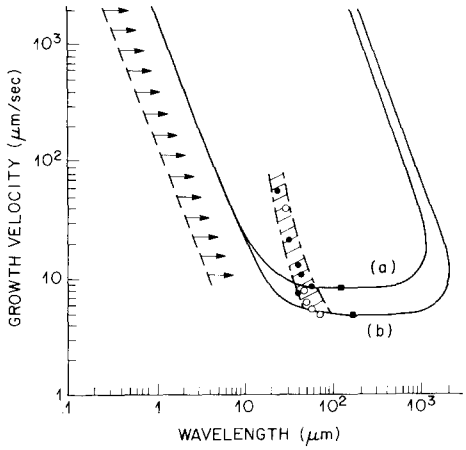

Fig. 3. Plot of the growth velocity versus wavelength for the experiments of de Cheveigné et al. [8]. The solid line marks the neutral stability wavelength as a function of the growth velocity for two values of the thermal gradient G. Experiments for (a) $G = 120\,^{\circ}\mathrm{C/cm}$ (●) and (*b*) $G = 70\,^{\circ}\mathrm{C/cm}$ (○) lie in the narrow shaded band. The dashed line indicates the minimum deep cell wavelength calculated in this paper, and the arrows illustrate that the matched asymptotic expansion employed in this paper is an expansion towards larger wavelength. See text.

field in front of the pattern. See section 2 for precise definitions.) In this limit a formal analogy with the equations describing viscous fingering in a Hele–Shaw cell [10,11] (the well-studied Saffman–Taylor problem) can be made. (See section 10 for details and comments on the limitations of this analogy.) Indeed Pelcé and Pumir [12] had already noted this connection, and there have been several attempts to analyze experimental data using the analogy to Saffman–Taylor fingers [13]. As shown later in this paper, for materials with small partition coefficients, we can extend the approach of Dombre and Hakim [10] to the experimentally relevant regime with Péclet numbers of order unity. Our approach reduces to theirs as $p \to 0$, where the restriction to small k is then not required, and we will therefore often refer to this particular branch of solutions we calculate as the Saffman–Taylor-like branch.

However, a steady state analysis alone can give no information about the *stability* of these solutions, and hence their relevance to real experiments. In fact there are strong indications that the wavelengths of experimentally selected patterns lie in a much narrower band than the width of the band for which a family (or families!) exists according to a simple steady state analysis.

Very near threshold, one typically expects [14] that the band of stable periodic nonlinear solutions lies within the planar instability band (near a supercritical (forward) bifurcation, this follows from the Eckhaus instability results for the amplitude equations [15]). Unfortunately, however, for directional solidification, the amplitude expansions [16] and bifurcation analysis [17] on which these conclusions are based are valid only extremely close to threshold, when $(V - V_c)/V_c \ll 1$. This is because the bottom of the neutral stability curve illustrated in fig. 3 is extremely flat in most cases, so expansion methods quickly break down as the velocity is increased. (The important exception [18] is the regime where the partition coefficient k is close to 1, as is the case for liquid crystals [19].) However, recent results by Brattkus and Misbah [20] on the stability boundary of strongly nonlinear solutions confirm that for their particular model the band of stable nonlinear solutions lies within, but is significantly narrower than, the planar instability band. The mechanism that governs the wavelength selection within the stable band they find still remains an unsolved problem.

We concentrate in this paper on the strongly nonlinear cellular patterns seen above threshold, avoiding both the initial planar instability and the flat region of the neutral stability curve just above threshold, as well as the dendritic regime seen at much higher pulling velocities. We have two main objectives. The first is to present a very simple stability criterion, based on ideas from the theory of constitutional supercooling (CS) that relates the stability of the tips of strongly nonlinear patterns to their position in the cell relative to that of the stable planar interface [21]. This predicted relationship can easily be tested experimentally, and is useful theoretically in determining whether a given steady state solution is likely to be stable. We expect it to be accurate for systems with small partition coefficients in the experimentally relevant case where curvature corrections to the concentration at the tip from the Gibbs–Thomson equation are small, so that one can think of the tip region as locally planar.

The basic idea is extremely simple. According to the theory of constitutional supercooling, the planar interface is stable provided that the impurity concentration in the melt *just in front* of the interface (determined from boundary conditions fixing both the concentration and the concentration gradient *at* the interface) does not fall into the (unstable) two-phase region as given by the phase diagram. At larger pulling velocities, the gradient at the planar interface increases. Eventually this causes the concentration just in front of the interface to fall in the two phase region, where, according to the CS picture, the planar interface goes unstable. In many experimentally relevant cases, the system restabilizes into nonlinear fingerlike patterns where the curvature corrections at the tips from the Gibbs–Thomson equation are very small. In this case it seems plausible that we can again apply the CS stability requirement *locally* in the tip region. This implies that the tip positions of *stable* non-linear patterns should move *up* relative to the steady state position of the plane (towards higher temperature, where less impurity is rejected at the interface) until the impurity concentration just in front of these nearly planar tips once again falls in the stable single phase region.

A quantitative treatment of this idea is given in section 3. There we introduce a dimensionless parameter ζ_t which provides a direct measure of the *local constitutional supercooling* (LCS) condition at the tip in terms of the tip position z_t, linearly related to ζ_t. To avoid supercooling, we need $\zeta_t \leq 0$. It is natural to conjecture that the operating point in real experiments is close to the region that requires the least forward motion, i.e., where $\zeta_t \approx 0$. We refer to this proposed *selection criterion* as the LCS criterion. Equations similar to the LCS criterion have in fact been used before, particularly in the dendritic regime found at still higher pulling velocity, or smaller temperature gradient [2,22–25]. However, the earlier derivations relied on somewhat ad-hoc matching arguments, and they attempted to predict a unique pattern spacing for a given set of experimental conditions, rather than determine which members of a family of solutions might be stable. To our knowledge, the derivation and interpretation of the LCS criterion in terms of stability concepts, and its particular relevance in the cellular regime has not been realized before. In appendix A we briefly discuss some of the earlier approaches.

There are immediate experimental and theoretical implications of this idea. On the experimental side, the predicted tip positions can easily be tested explicitly. From the very limited amount of data on the tip position in the cellular regime available in the literature, there is in fact some indication that a relation of this kind holds true to a reasonable approximation [21]. See section 10 for further discussion.

The theoretical implications of the LCS idea for cellular patterns can best be seen in connection with the second main objective of this paper. That is to present a detailed theory for a particular class of steady state solutions – both finite amplitude cells and cells with deep grooves – for which a very simple (and, in some limits, exact) analysis can be carried out [26].

The finite amplitude shapes are solutions resembling those in fig. 1a, but where the concentration field remains essentially one-dimensional and dominated by the simple exponential fall-off found at the planar interface, even though the interface itself is far from planar. The theoretical analysis becomes exact in the limit that the partition coefficient $k \to 0^+$, where the solid rejects almost all impurities, but we will provide evidence that this branch can be accurately calculated perturbatively for small but realistic values of k, say $k \lesssim 0.15$. A wide range of other parameters can be studied, including, in particular, Péclet numbers of order unity.

We also analyze a branch of solutions with deep grooves, resembling the ones in fig. 1b or fig. 2, using what is essentially a modern and more rigorous version of a classical approach long studied by material scientists [2,3]. The idea is to approximate the fingerlike solutions in two different regions – in the tip region and in the deep grooves, and then somehow join these descriptions together in an intermediate "matching region" below the tip.

To carry out this program, of which a brief description appeared in ref. [26], we first examine the interface shape in the grooves. Away from the

tip we can exploit the straightness and narrowness of the grooves to give a systematic perturbation treatment of the interface shape. These results can be directly compared to experiment. When curvature effects can be neglected, the solution we find reduces to the classical Scheil shapes [2,3,27,28]. However, we derive new terms [26,29] involving the curvature that are essential to describe how the interface bends away from the nearly straight Scheil shapes and thus can smoothly join some tip solution. Our (lowest order) description of the groove region should be quite accurate in many cases, and can be improved systematically.

Our treatment of the other two aspects of the matching approach turns out to be less generally valid, though it does accurately describe a particular branch of steady state solutions. In essence, we use the upper portion of the finite amplitude solutions discussed above to describe the region close to the tip. Then, in the experimentally relevant case where the grooves remain narrow even rather near the tip, it seems very plausible, following Dombre and Hakim [10], to assume there exists just below the tip a single "matching region" where both the tip and tail solutions can be connected together, thus producing a globally acceptable solution [30]. Dombre and Hakim [10] introduced a systematic *asymptotic matching* procedure that yields a perturbation expansion whose small parameter, ϵ, equals the width of the grooves in the matching region relative to the pattern wavelength. As $\epsilon \to 0$, the matching method gives an essentially exact treatment of this branch of solutions with deep grooves.

The solutions this method produces illustrate in a very clear way two central themes that recent work in DS has established: (i) the critical importance of the surface tension terms in the interface boundary condition in setting the overall scale of interface patterns and (ii) the existence of a family of steady state solutions with varying wavelengths. Although some numerical work is required, computations are sufficiently fast and simple that the effects of varying a wide range of experimental parameters can easily be studied.

In addition to the above, mainly pedagogical, virtues we now have the opportunity to make direct comparisons between our finite Péclet number solutions and the experimental patterns. Unfortunately, here the limitations in the matching methods become apparent. We had expected that our steady state analysis would produce a band of permitted solutions, of which only some narrow region would be experimentally stable. However, it turns out that *all* the solutions that we can calculate perturbatively have wavelengths much smaller than experiment, by about an order of magnitude.

One might be inclined to attribute much of this discrepancy to lack of knowledge of precise values for experimental parameters or oversimplifications in the theoretical model (e.g., a purely two-dimensional model is assumed, while de Cheveigné et al. [8] have shown there is a significant dependence in the experimental threshold velocity on cell thickness).

However, the matching approach is based on an expansion for fixed velocity V away from the $\epsilon = 0$ fingerlike solution with vanishingly small grooves width, i.e., that solution with the smallest possible wavelength. This is indicated in fig. 3, where the dashed line corresponds to these minimum wavelength solutions as a function of V. The small ϵ solutions accessible with this expansion, indicated by arrows, are seen to fall *outside* the planar instability band calculated using the same (theoretical) parameter values. Thus our previous discussion strongly suggests that the solutions found with this expansion can all be expected to be *unstable*. The longer wavelength solutions selected in experiment lie well *within* the planar instability band.

Indeed, the experimentally selected solutions have sufficiently long wavelengths λ that curvature corrections from the Gibbs–Thomson equation are very small near the tips. (The curvature is roughly proportional to λ^{-1} in the cellular regime.) In such a case, we expect our LCS stability criterion $\zeta_t = 0$ should apply as a good approximation to them. In contrast, the small ϵ solutions obtained by the matching method have ζ_t of O(1) and much smaller wavelengths λ, and for them, curvature effects are much more important.

The simplest interpretation of all these facts is that the matching theory describes a branch of steady state solutions that is *different* from the

experimentally relevant one. We argue below that this is the case, and identify the critical step in the matching theory that may lead us to find (only) the unstable branch. This appears to be an unavoidable consequence of the basic assumption that there exists a single matching region, controlled by the groove width ϵ, which can be made arbitrarily small. As a result, the predicted values of ζ_t for small ϵ are O(1), whereas LCS leads us to expect that $\zeta_t \approx 0$! Thus if experimental tips do have $\zeta_t \approx 0$, then they will be inaccessible by the present matching approach. Unfortunately, it is also not easy to see how the matching methods can be modified to apply in the case $\zeta_t \approx 0$.

The fact that the cell shapes we can calculate perturbatively have wavelength much smaller than the selected ones also bears directly on other theoretical results. As mentioned above, a number of studies [11–13,29,31] have exploited the fact that in the small Péclet number limit, the directional solidification problems can be formally mapped onto the viscous fingering problem, for which shape selection is well understood. Wide viscous fingers (i.e. those with narrow "grooves") *are* correctly described by the perturbative methods developed by Dombre and Hakim [10], and they correspond, loosely speaking, to the *large* surface tension limit. On the other hand, while most experimentally observed solidification cells typically do have narrow grooves, at the same time they have small enough tip curvature that surface tension effects can be viewed as a *small* correction. This seems to contradict the simple mapping [12,10,29,31] onto the viscous fingering problem, which associates narrow grooves with large surface tension effects. Therefore, even in the small Péclet number limit, we believe that experimental fingers may well belong to a different branch, and one to which the formal analogy to the viscous fingering problem does *not* apply. This will be discussed in detail in section 10.

It is interesting to note that a similar situation has been argued to occur for dendritic growth in a channel [32], which may be viewed as the limit of vanishing temperature gradient in DS. Here, two branches of steady state solutions are believed to exist [33], a Saffman–Taylor like branch and a *different* one that for wide channels reduces to free dendrite-like behavior. In this case, the Saffman–Taylor branch contradicts physical intuition in that cells at small undercoolings are thin and cells at large undercooling wide, and there are several indications that the experimentally relevant branch is the dendrite-like one. See section 10 for further details.

Thus, despite the fact that our matching theory does not seem to describe real experimental patterns, it is not without interest. The theory does accurately describe a branch of highly nonlinear steady state solutions. It clearly focuses attention on a number of unresolved issues that so far have remained largely unnoticed. And it was through examination of the experimental shortcomings of the matching predictions that we were first led to the simple LCS stability criterion, which we expect to apply reasonably well to experimental cellular patterns. If this is borne out, the LCS criterion will also be a useful guide in assessing the relevance of theoretical cell shapes to experiments.

Before turning to the detailed calculations, let us summarize our main results and conclusions for the matching solutions.

(1) For systems with small k, we can calculate the properties of a particular continuous branch of steady state solutions describing cellular profiles with deep narrow grooves. The Péclet number dependence of these solutions is weak, and for $p \to 0$ they reduce to the Saffman–Taylor-like solutions found earlier by Dombre and Hakim [10]. The variation in wavelength of this branch is parametrized in the matching theory by the relative groove width ϵ near the tip, or, more convenient to experiment, by the dimensionless LCS parameter ζ_t giving the tip position (see sections 9 and 10, and fig. 13).

(2) A fundamental assumption self-consistently satisfied by these solutions is the existence of a single matching region controlled by the small parameter ϵ where deep narrow grooves can be matched to a particular class of finite amplitude cellular solutions describing the fingertip region. These finite amplitude solutions have wavelength lying *outside* the planar instability band and evolve from the (infinitesimal amplitude) neutrally stable modes forming the short wavelength side of the

planar instability band (i.e. the left hand solid curve in fig. 3). These solutions have a regular expansion in powers of k. The fingerlike solutions with narrow grooves (small ϵ) resulting from the matching also have wavelengths lying outside the planar instability band and have values of ζ_t of order unity (see sections 9 and 10).

(3) Most numerical studies, using the same two-dimensional model we consider here, find narrow-grooved fingerlike patterns, but with wavelength lying *inside* the planar instability band. These solutions are found well above threshold and evolve from small amplitude cells with wavelengths lying inside the planar instability band, presumably related for small k to the cells studied by Sivashinsky [16] and others. The latter bifurcate off from the *center* of the planar instability band (indicated by the square in fig. 3), and do not have a regular k expansion. The contrast with the matching solutions discussed in (1) is evident (see section 10).

(4) Most experimental patterns also have narrow grooves, but with wavelength lying inside the planar instability band. In the few cases where experimental data on the tip position is available, small values of ζ_t are found, in qualitative agreement with the LCS stability criterion $\zeta_t \approx 0$. This implies that the tips of experimentally selected patterns have moved up substantially in the temperature gradient relative to the planar position (see section 10 and fig. 13).

(5) In contrast, the matching solutions for small ϵ have ζ_t of order unity, i.e. their tips remain close to the planar position. More detailed experimental measurements of ζ_t would be extremely useful to determine the accuracy of the LCS ideas (see section 10).

(6) The analysis of Brener et al. [33] for crystal growth in a channel, as well as arguments by Ungar and Brown [4], again suggest the existence of a branch of steady state solutions in DS other than the ST branch. The analytic mapping of the $p \to 0$ DS equations to the ST problem breaks down near the LCS line $\zeta_t \approx 0$. Thus we argue that the matching solutions lie on a different, and physically irrelevant, branch of steady state solutions for DS (see section 10).

While the matching ideas used in this paper makes systematic many of the earlier approaches used by material scientists [2,3], the mathematical techniques (asymptotic matching [30]) as well as the results and their implications do not appear to be widely known in this community. We will thus attempt to give a pedagogical and rather detailed account of them here, which also will focus on their limitations. We also give some details about preliminary steps involving the introduction of dimensionless units and other notational matters, since different conventions adopted by various authors have caused some confusion in the literature. Readers who are familiar with the problem and who are only interested in the main results and their implications can proceed directly to sections 3, 6, 7.4, 9 and 10.

The plan of the paper is the following. In section 2, we review the equations for directional solidification. We use a simple two-dimensional model, the one-sided (solutal) model [1], which is still realistic enough to compare to experiments, and which has been extensively studied numerically. In this model, convection in the liquid is ignored and the imposed temperature gradient is assumed to be unaffected by the latent heat released or by changes in the interface shape. These often are rather accurate approximations. We generally ignore diffusion in the solid, taking the limit where the diffusion constant ratio $\beta \equiv D^s/D$ tends to zero. Contrary to the conclusion the casual reader might get from ref. [34], we argue that the one-sided model offers an accurate description of many features of interface patterns seen in realistic systems with β small but non-zero. However, a notable exception where the one-side model must break down is in the reentrant part of the bubble closure in fig. 1b. This will be discussed in appendices B and C.

In section 3, we give a detailed discussion of the LCS stability criterion, together with its limitations. In section 4, we discuss the various dimensional parameters that characterize a DS experiment, and the fundamental dimensionless ratios that most theories use. We choose a length scale essentially equal to the (lower) neutral stability wavelength λ_s (the left-hand solid line in fig. 3), and argue that this scaling facilitates comparison between theory and experiment. In particular, this

scaling helps us assess the relative importance of the curvature corrections in the Gibbs–Thomson boundary condition at the tips of real experimental patterns and hence the accuracy of the LCS condition. In section 5, we derive exact equations expressing flux conservation which serve as a useful starting point to yield approximations for the tail (section 6) and for the tip (section 7). After a discussion of the behavior of the resulting finite amplitude cellular solution in section 7, we then turn in section 8 to the asymptotic matching analysis which yields approximate shape expressions for cells with deep grooves. The results of this analysis are presented in section 9, while in section 10 we discuss in detail the implications of our results and how they compare to experiments and other theoretical work.

2. Equations for the one-sided model

We consider the typical experimental setup where a thin ampoule initially filled with a binary melt with impurity concentration c_∞ is pulled through a temperature gradient established by fixed hot and cold contacts. The gradient is large enough that solidification must occur as the melt is pulled from the hot to the cold region of the cell. The impurity concentration c in the melt obeys the diffusion equation

$$\frac{\partial c}{\partial t} = D \nabla^2 c, \tag{2.1}$$

where c tends to c_∞ far in front of the interface. In principle, there is a similar equation in the solid involving D^s, the diffusion constant in the solid. However, for most metallic or plastic crystal solidification systems the diffusion constant ratio $\beta \equiv D^s/D$ is of order of or smaller than 10^{-2}, and in many expressions it is a good approximation to ignore diffusion in the solid entirely, thus arriving at the *one-sided model*, with $D^s \equiv 0$. The one-sided model is much simpler to treat analytically, and we find that it offers an accurate description of many features of interface patterns seen in realistic systems with β small but non-zero. In appendices B and C we discuss cases such as that of a multiple-valued or reentrant interface where this approximation must break down.

Most systems with small β also have relatively small values of the partition coefficient k, since impurities that do not diffuse well in the solid tend to be rejected on solidification. Thus the limit of small β and k analyzed here is relevant to many experiments. The main exception concerns liquid crystals, where both β and k are of order unity [19]. Here the deep grooved patterns of primary interest to us in this paper are usually not found.

At the interface we assume local thermodynamic equilibrium as given by the Gibbs–Thomson equation, so that the temperature at an interface with impurity concentration c_i and curvature κ (taken positive when the solid bulges into the liquid) is

$$T_i(c_i, \kappa) = T_L(c_i)(1 - \hat{d}\kappa) \tag{2.2}$$

$$\approx T_M - m_L c_i - T_M \hat{d}\kappa. \tag{2.3}$$

Here $T_L(c_i)$ is the (liquidus) temperature for a planar interface with impurity concentration c_i as given by the phase diagram. (The subscript i will in general denote a quantity evaluated at the interface; we use a superscript s to denote the solid phase.) In (2.3) we have assumed a simple linear phase diagram as in fig. 4a, appropriate for dilute solutions, and expanded about the pure solvent at

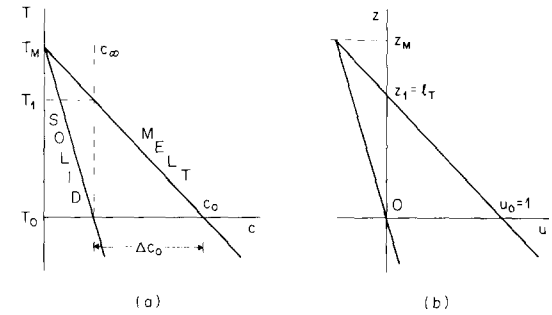

Fig. 4. (a) Phase diagram illustrating the various temperature and concentration parameters defined in the text. (b) Phase diagram in terms of the dimensionless concentration variable u. Along the vertical axis, the temperature has been eliminated in favor of the height variable z with the aid of (2.6). The position $z = l_T$ is the point where $T = T_1$ in (a), and $z = 0$ denotes the steady state planar interface position where $c_\infty = kc_0$.

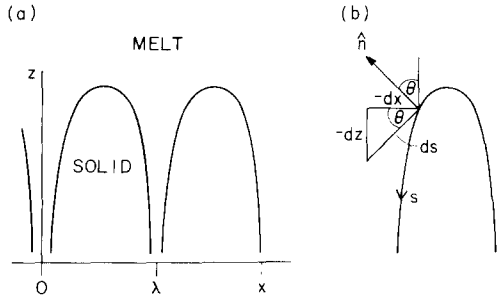

Fig. 5. Illustration of our coordinate conventions.

T_M to first order in c and κ, with [36] $m_L \equiv |dT_l/dc|$.

Strictly speaking, if crystal growth is to occur, there must be some kinetic undercooling [1], but this is usually very small for growth in the cellular regime. The local equilibrium assumption (2.3) generally produces little quantitative error and is standard for the theoretical model studied herein. See, however, section 10 for some remarks about the possible importance of interface kinetics in certain limiting cases.

Surface tension corrections show up in the term $\hat{d}\kappa$ in (2.3). For cubic crystals, we assume the specific form $\gamma(\theta) = \gamma_0(1 + \bar{\alpha}_4 \cos 4\theta)$ for the angular dependent surface free energy, but our results can easily be generalized to arbitrary $\gamma(\theta)$. Here θ is the angle between the interface normal and the z axis, which is taken along the pulling direction. See fig. 5. The quantity $\hat{d}(\theta)$ appearing in (2.2) and (2.3) is proportional to $\gamma + d^2\gamma/d\theta^2$, and can be written [37]

$$\hat{d}(\theta) = \hat{d}_0(1 - \alpha_4 \cos 4\theta). \tag{2.4}$$

Here $\hat{d}_0 \equiv \gamma_0/L$ is the *intrinsic capillary length*, with L the latent heat per unit volume and $\alpha_4 = 15\bar{\alpha}_4$ for the specific form of $\gamma(\theta)$ assumed above. In most materials $\hat{d}_0$ is of the order of atomic dimensions, and hence much smaller than the radius of curvature of typical interface patterns. Nevertheless, the curvature correction in (2.3) will turn out to play an important role in establishing the overall scale of patterns found in a DS experiment. Although the anisotropy $\bar{\alpha}_4$ in the surface tension is generally rather small (of the order of a few percent or less), we see that the anisotropy α_4 in $\hat{d}(\theta)$ is much larger. However, unlike what is believed to be the case for free dendritic growth [37], anisotropy is not an essential feature for the existence of steady state patterns in DS. Thus, for notational simplicity in the equations that follow, we consider the case $\alpha_4 = 0$ or $\hat{d} = \hat{d}_0$, although we will also report some results of calculations with α_4 nonzero.

A second boundary condition expresses local conservation of impurities:

$$V_n \Delta c_i = -D(\hat{n} \cdot \nabla c)_i. \tag{2.5}$$

Here V_n is the normal component of the interface velocity, $\Delta c_i \equiv c_i - c_i^s$ the "impurity surplus" rejected into the liquid as the interface advances, and $(\hat{n} \cdot \nabla c)_i$ the normal component of the concentration gradient at the interface. Eq. (2.5) equates the rate at which impurities are rejected at the interface to the diffusion flux into the liquid. Again we have assumed that the one-sided model is accurate, and ignored any diffusion flux into the solid.

We assume that the contacts set up a *linear* temperature gradient, thus neglecting the generally small corrections due to latent heat generated at the interface. Then the temperature field in a frame where the contacts are at rest is simply

$$T = T_0 + Gz, \tag{2.6}$$

where T_0 is a reference temperature (chosen later to equal that of the steady state planar interface) and G the imposed temperature gradient. Evaluating (2.6) in the liquid at the interface and combining with (2.3) gives an equation describing the variation of the impurity concentration as a function of interface position and curvature,

$$c_i = c_0 - (G/m_L)z_i - (\hat{d}_0 T_M/m_L)\kappa, \tag{2.7}$$

where c_0 is the liquidus concentration at temperature T_0. In the same way, we can derive an equation for the concentration c_i^s in the solid at the interface. Using (2.7), the result can be written

$$c_i^s = kc_i, \tag{2.8}$$

where, for the simple linear phase diagram of fig. 4, the *partition coefficient* k is a constant,

$$k = m_L/m_S. \tag{2.9}$$

Graphically, k is the ratio of the liquidus to the solidus slopes.

We are interested in *steady state* solutions of (2.1), (2.5) and (2.7) and note that the patterns are stationary in a frame where the contacts are at rest, i.e., a frame moving at velocity V in the $+z$ direction with respect to matter in the sample. We use this moving frame in all that follows. For such stationary patterns $V_n = V \cos\theta$ (see fig. 5), and the left-hand side of (2.1) evaluated in the moving frame becomes $-V\,\partial c/\partial z$.

The simplest solution of the steady state equations describes a planar interface, for which the concentration field satisfies

$$c = (c_0 - c_\infty)\, e^{-z/l_D} + c_\infty. \tag{2.10}$$

Here we have chosen $z = 0$ as the location of the planar interface, where by definition $c_i = c_0$ and $T_i = T_0$, and defined the *diffusion length*

$$l_D \equiv D/V. \tag{2.11}$$

To determine c_0 in terms of experimental parameters, we use eq. (2.5) and find

$$c_0^s = kc_0 = c_\infty. \tag{2.12}$$

Thus the planar interface is located at that point in the cell where the impurity concentration incorporated into the solid, kc_0, equals the limiting impurity concentration c_∞. This global conservation condition is required for steady state planar growth. See fig. 4.

We use the planar solution to help define a dimensionless concentration field, u, scaled so that typical variations are of order unity:

$$u \equiv (c - c_\infty)/\Delta c_0, \tag{2.13}$$

where, using (2.12), $\Delta c_0 \equiv c_0 - c_0^s = c_0 - c_\infty$. Clearly $u_0 = 1$ and $u_0^s = 0$ from (2.12), and in general $u = 0$ far in front of the interface. See fig. 4b, where the phase diagram is replotted in terms of the variable u and the position z in the cell, using (2.6).

Eqs. (2.1), (2.3) and (2.5) in the steady state can then be put into the reduced form [1,26]

$$\nabla^2 u + \frac{1}{l_D}\frac{\partial u}{\partial z} = 0, \tag{2.14}$$

$$u_i = 1 - z_i/l_T - d_0\kappa, \tag{2.15}$$

$$\Delta u_i \cos\theta = -l_D[\hat{n}\cdot\nabla u]_i. \tag{2.16}$$

Here

$$\Delta u_i \equiv u_i - u_i^s = u_i - k(u_i - 1) \tag{2.17a}$$

$$= 1 - (1-k)(z_i/l_T - d_0\kappa), \tag{2.17b}$$

is the dimensionless "impurity surplus" and we have used (2.12), (2.13) and (2.15) to arrive at (2.17b). Eq. (2.15) follows directly from (2.7) and introduces two fundamental lengths [38]: the *thermal length*,

$$l_T \equiv m_L \Delta c_0/G, \tag{2.18}$$

and the *chemical capillary length*,

$$d_0 \equiv \hat{d}_0 T_M/m_L \Delta c_0. \tag{2.19}$$

The chemical capillary length d_0 is normally much larger than $\hat{d}_0$. From (2.15) and (2.13) we see that the temperature T_1 at $z = l_T$ is such that the *liquidus* concentration equals c_∞, while from (2.12) the temperature T_0 and the location $z = 0$ is fixed by the requirement that the *solidus* concentration equals c_∞. See fig. 4a. Note from (2.15) that the equation for the liquidus line in the modified phase diagram in fig. 4b is

$$u_L(z) = 1 - z/l_T. \tag{2.20}$$

Since the curvature κ_t is greater than zero at the tip of a solidification pattern, and we expect no "concentration deficits" with $u < 0$ in front of a steady state pattern, eq. (2.15) shows that the tip position z_t of any such pattern is such that $z_t < l_T$. In the next section we discuss the LCS stability criterion that sets an approximate bound on the position z_t of many experimental patterns.

When diffusion in the solid can be ignored, we can relate the concentration field in the solid to that "frozen in" at the interface above. In the steady state, eqs. (2.8) and (2.13) then imply

$$u^s(x, z) = k\big[u(x, z_i(x)) - 1\big], \tag{2.21}$$

where $u(x, z_i(x)) = u_i$ gives the concentration in the melt at interface position $z_i(x)$. As a result, we need explicitly consider only the field u in the liquid and at the interface, as in eqs. (2.14)–(2.16). Clearly, however (2.21) must break down if we have a multiple valued or reentrant interface, where for a given x there are two or more values

of $z_t(x)$. This is discussed in appendices B and C, but for now we will assume the patterns are such that there exists a single-values interface for which the one-sided model with $D^s = 0$ remains accurate.

3. Interface stability and constitutional supercooling

The first successful stability criterion for a planar interface in DS was based on the idea of constitutional supercooling [1–3]. As suggested in the introduction, we can argue as follows. The phase diagram (see fig. 4a) applies to *stationary* planar interfaces and delineates the two phase region between the liquidus and solidus curves where a stable (one-phase) liquid at a particular T and c cannot exist. The basic idea of constitutional supercooling (CS) is [1–3] that in the steady state we can assume local equilibrium and apply these same thermodynamic concepts to the *moving* planar interface and to the *melt just in front* of the interface. This idea was implicit in rewriting the phase diagram as a function of z in fig. 4b.

In general, we assume local thermodynamic equilibrium *at* the interface by using the Gibbs–Thomson boundary condition (2.15). Constitutional supercooling makes the very plausible assertion that the moving planar interface remains stable as long as the melt just in front of the interface also satisfies the thermodynamic requirement for single phase stability: the concentration there should not fall into the two phase region of the phase diagram.

Since the concentration at the interface is on the liquidus line from (2.15), the CS condition for stability of the liquid just in front of the interface reduces to the following requirement. The (dynamical) gradient $|\mathrm{d}u/\mathrm{d}z|_t = \Delta u_t/l_D$ determined from the boundary condition (2.16) must not exceed the liquidus slope $|\mathrm{d}u_L/\mathrm{d}z| = 1/l_T$ given in fig. 4b or eq. (2.20), where the temperature dependence of the phase diagram in fig. 4a is reexpressed as a function of position z in the cell. This criterion can be reexpressed as

$$\nu(\Delta u_t) \le 1, \tag{3.1}$$

where we define a basic dimensionless control parameter ν:

$$\nu \equiv l_T/l_D = Vm_L\Delta c_0/GD. \tag{3.2}$$

Note that ν is directly proportional to the velocity V. The usual CS criterion for *instability* of the plane follows from (3.1) where we note that *global* conservation requirements force the plane to be located at $z_t = 0$, where $\Delta u_t = 1$. (See fig. 4b or eq. (2.17b) and the discussion after eq. (2.12).) Thus, as V is increased the planar interface at $z = 0$ is predicted to be stable until a critical value of V is reached such that

$$\nu_c^{CS} = 1. \tag{3.3}$$

This criterion is surprisingly accurate, given the simplicity of the CS argument. For materials with small k, the fundamental linear stability analysis [1] predicts only small changes in the critical value of ν, i.e., $\nu_c \approx 1$. At the very least, the CS theory provides a very useful "rule of thumb" for estimating planar interface stability [1].

However, the arguments leading to (3.1) seem nearly as plausible as before when applied *locally* to the melt in front of the tip of many (non-planar) patterns, provided that the curvature corrections in (2.15) are small. In particular, we need to use only the *boundary conditions* (2.15) and (2.16) and the *local symmetry* in the tip region (nearly planar, with $\theta_t = 0$) to arrive at (3.1) with $\Delta u_t = \Delta u_t$, the impurity surplus at the tip. When curvature corrections to Δu_t in (2.17b) are small, eq. (3.1) can be reexpressed as

$$\zeta_t \equiv (\nu - 1) - (1 - k)z_t/l_D \le 0. \tag{3.4}$$

Eq. (3.4) predicts that the tip position z_t of stable patterns with $\nu > 1$ must move *up* in the cell, relative to the planar position at $z = 0$, until the smaller impurity surplus Δu_t allows (3.1) or (3.4) to hold true. It is natural to conjecture that the operating point in real experiments should be close to the one that requires the least forward motion, i.e., the region where $\zeta_t \approx 0$. We refer to this condition as the LCS criterion.

Note also that just as the Mullins–Sekerka instability of the plane is a finite wavenumber instability [1], we expect that the instability of

cells predicted by LCS for $\zeta_t \gtrsim 0$ actually corresponds to a finite wavenumber instability [39]. This is indeed confirmed by a more careful analysis [21], which also shows that the LCS criterion $\zeta_t = 0$ gives an *upper bound* to the distance z_t that the tips of patterns have to move up to regain stability. For a periodic array of cells with $\zeta_t \approx 0$, we envision that the instability in practice corresponds to a mode in which some of the cells move up slightly, while others stay behind and subsequently get pinched off.

Ref. [21] also shows that curvature corrections neglected in LCS become more important at larger ν. Indeed corrections to the LCS picture must surely be taken into account at large $\nu > 1/k$ (usually in the dendritic regime), since (3.4) combined with (2.15) would then predict $z_t > l_T$, thus implying an unphysical "concentration deficit" at the tip with $u_t < 0$. However, for small k and ν in the cellular regime, corrections to LCS appear to be small.

Of course, these arguments are only suggestive. The LCS condition (3.4) is not exact, even for the plane at $z = 0$. However, in that case we can compare its predictions to those of an exact linear stability analysis. For materials with small partition coefficient and small $\beta = D_s/D$ it does give a very accurate estimate. Similarly, we expect that the linear stability analysis of the fingertip region of many nonlinear patterns would agree rather well with the predictions of (3.4). We hope this will be investigated in the future. Measurements of the tip temperature similar to those by Esaka and Kurz [40] yield all the necessary information to determine ζ_t (see section 10 for a more detailed discussion of these experiments).

As shown in appendix D, one can define a measure of constitutional supercooling for a general point near the interface of a fingerlike pattern, although the analogy to the planar case is less compelling when θ_i is non-zero. Using this, we can establish the general validity of the frequently made assumption [2,25,28] that the constitutional supercooling in the grooves is small. However, this fact places no constraints on the absolute location of the pattern in the experimental cell. In contrast, the requirement of small supercooling near the *tip* with $\zeta_t \approx 0$ does approximately fix z_t.

As we will see in the rest of this paper, the condition $\zeta_t \approx 0$ will also have important implications for the validity of various matching theories for DS. To analyze these questions in more detail, we first discuss in the next section a choice of length scale in the theory that renders eqs. (2.14)–(2.16) dimensionless. Our choice will be particularly useful in helping to determine the relative importance of the curvature terms in (2.15) and hence the applicability of the LCS criterion.

4. Experiments and theoretical parameters

There are many parameters that can be varied in a directional solidification experiment. The choice of the solvent and impurity system fixes the material parameters k_v, T_m, $\hat{d}_0$, D and m_L. In principle, one can still vary the limiting impurity concentration in the melt c_∞, the temperature gradient G, and the pulling velocity V, to produce a variety of patterns, whose properties can be characterized in terms of the parameters l_D, l_T and d_0 given in eqs. (2.14)–(2.16). We consider here the usual experimental set up where c_∞ and G are fixed and V is increased above the threshold velocity V_c to produce instabilities in the planar interface.

In such an experiment, the choice of c_∞ fixes c_0 and the location $z = 0$ from eqs. (2.11) and (2.12), as well as the chemical capillary length d_0 from eq. (2.19). Choosing G then determines the thermal length l_T from eq. (2.18). As V is increased, the diffusion length $l_D = D/V$ decreases at fixed d_0 and l_T. We are interested in properties of the periodic cellular patterns that emerge, in particular their wavelength λ and parameters that characterize their shape such as the tip position and the groove width.

We can choose one of the four lengths d_0, l_T, l_D, and λ (or some combination thereof) as a unit of length and thus characterize the results of an experiment in terms of fundamental dimensionless ratios. The following choices are often made.

One basic control parameter ν describes how far the system is from the instability threshold; it

has already been mentioned in section 3, where we defined

$$\nu \equiv l_T/l_D = Vm_L\Delta c_0/GD. \tag{4.1}$$

Since the constitutional supercooling instability criterion $\nu_c = 1$ is usually very accurate, we can think of ν as the ratio of the pulling velocity V to the threshold velocity V_c. The cellular regime of interest to us in this paper is found at larger ν with $\nu - 1$ of O(1); at still larger pulling speeds $\nu \gtrsim 10$ a dendritic regime is usually found. We will not consider the latter regime in this paper.

The resulting patterns are often characterized by the *Péclet number p*, where

$$p \equiv \frac{\lambda}{2l_D} = \frac{\lambda V}{2D} \tag{4.2}$$

relates the scale of the pattern (the half wavelength) to l_D, the typical range of the diffusion field in front of the tips. Experimental cells can have Péclet numbers as large as O(1).

These ratios [38] arise naturally in the resulting dimensionless equations when l_D is chosen as the unit of length. Another common choice in theoretical work is λ itself. However both of these choices, while perfectly consistent and offering some theoretical advantages, can cause some inconvenience when comparing theory and experiment. Thus the choice l_D gives a scale that is not obviously the size of a typical pattern.

On the other hand, the choice λ gives a length scale that by definition is the size of a pattern. However, conceptually this is somewhat dissatisfying since that scale is not fixed in advance: the prediction of λ is actually a goal of the analysis. With this choice it becomes natural to report theoretical results in terms of a dimensionless parameter σ relating the surface tension to the pattern wavelength. See eq. (9.1) below. Using this, it is possible to extract the actual (dimensional) value of λ.

We make here another choice of length scale which avoids some of these problems. As illustrated by fig. 3, most experimental cellular patterns have wavelengths λ that are some small multiple of the (lower) neutral stability wavelength λ_s evaluated at the appropriate pulling velocity. Except for the very flat part of the curve in fig. 3 extremely near threshold, which we do not consider henceforth, λ_s is essentially independent of the value of the partition coefficient k (at least for small k) and is accurately approximated by $\lambda_s(k = 0) \equiv \lambda_s^0$ where [41]

$$\lambda_s^0 = 2\pi\left(\frac{\nu d_0 l_D}{\nu - 1}\right)^{1/2}. \tag{4.3}$$

(This result arises [1] when one considers a small interface perturbation of the form $\exp(iqx + \omega t)$; by definition $q_s \equiv 2\pi/\lambda_s$ satisfies $\omega(q_s) = 0$.) Thus a scale related to λ_s^0 seems appropriate. In the following, we take the half wavelength $\lambda_s^0/2$ as the unit of length. Measured in these units, the *dimensionless* half wavelength $a \equiv (\lambda/2)/(\lambda_s^0/2)$ of the experimental patterns of de Cheveigné et al. [8] is some small multiple of unity. We expect this result to be true for most experiments, where we assume that the selected patterns have wavelengths falling within the planar instability band towards the left-hand side. Note from (4.3) the well-known result that the experimental patterns are found on a length scale that is intermediate between the (usually small) scale d_0 set by surface tension forces and a macroscopic scale l_T or l_D.

Our basic equations (2.14)–(2.16), written with $\lambda_s^0/2$ as unit of length, then have the dimensionless form

$$\nabla^2 u + p_s\frac{\partial u}{\partial z} = 0, \tag{4.4}$$

$$p_s(\Delta u_i)\cos\theta = -(\hat{n}\cdot\nabla u)_i, \tag{4.5}$$

$$u_i = 1 - \frac{p_s}{\nu}\left(z_i + \frac{\nu - 1}{\pi^2}\kappa\right), \tag{4.6}$$

where we have defined

$$p_s \equiv \lambda_s^0/2l_D, \tag{4.7}$$

in analogy to the usual Péclet number p, in eq. (4.2). In general we use the subscript s to denote quantities associated with the stability length. It should not be confused with the superscript s denoting the solid. Note that $p = p_s a$. (To obtain the corresponding equations used in our earlier work [21,26] with the half wavelength $\lambda/2$ taken as unit of length, replace in the above equations p_s

by p and $\pi^{-2} \equiv \sigma_s$ by σ, as defined in eq. (9.1) below.)

For simplicity in notation, we do not indicate by a special symbol in eqs. (4.4)–(4.7) and those that follow that the coordinates x and z are now dimensionless, with $\lambda_s^0/2$ as unit of length. The presence of other dimensional (e.g., l_D and l_T) or dimensionless (e.g., p_s, ν) parameters in the equations themselves will indicate the proper dimensions to assign to the coordinates. Note also that throughout this paper, λ and λ_s^0 will always denote the *dimensional* wavelengths, whereas a denotes the *dimensionless* half wavelength of a pattern.

Finally note that in experiments where the selected wavelengths fall inside the planar instability band, we have $a > 1$. The curvature at the tip of these patterns is very roughly given by a^{-1}. (This estimate is exact for fingers of vanishing groove width whose tips are semicircles.) The curvature correction term in (4.6) is thus approximately given by $(\nu - 1)p_s/(\nu\pi^2 a)$. In the cellular case we have $\nu - 1$ of O(1), and usually $p_s \lesssim 1$, so curvature effects are numerically small in (4.6), unless the tips have moved so high that u_i is very near zero.

5. Flux conservation

A study of the impurity flux provides a powerful means of analyzing eqs. (4.4)–(4.6). The (dimensional) impurity flux in the moving frame at any point in the fluid is given by

$$\boldsymbol{J} = -D\,\nabla c - Vc\hat{z}, \tag{5.1}$$

where the first term is the usual diffusion flux, and the second is the "convective" flux of impurities in our moving reference frame induced by the constant pulling velocity V in the $-z$ direction. In the solid phase, by assumption $D^s = 0$, so that only the second term remains.

For a spatially periodic steady state pattern, it is clear that the impurity flux in the $-z$ direction (i.e., $-\boldsymbol{J}\cdot z$) integrated over any horizontal line segment extending from the center of a groove to the center of the pattern must be constant, independent of the position of the segment, since no net flux can escape through the vertical lines of symmetry. See fig. 5.

Using the notation of (4.4)–(4.6), a dimensionless measure of this integrated flux in the melt for $z > z_t$, with z_t the tip position of a pattern, is

$$F(z) = \int_0^a \mathrm{d}x \left(u + p_s^{-1} \frac{\partial u}{\partial z} \right), \tag{5.2}$$

where z denotes the segment position, a is, as before, the dimensionless half wavelength, and we have noted that $\nabla u \cdot \hat{z} = \partial u/\partial z$. Far in front of the interface we know that $u = \partial u/\partial z = 0$, so conservation of impurities in the steady state requires that $F(z) = 0$ everywhere. If we consider an arbitrary line segment whose vertical position z satisfies $z < z_t$ we have similarly

$$F(z) = 0 = \int_0^{x_i} \mathrm{d}x \left(u + p_s^{-1} \frac{\partial u}{\partial z} \right) + k \int_{x_i}^a \mathrm{d}x \left[u(x, z_i) - 1 \right], \tag{5.3}$$

where we have used eq. (2.21) to rewrite the impurity concentration in the solid in terms of that found at the fluid interface directly above. Here $x_i \equiv x_i(z)$ and $z_i \equiv z_i(x)$ give the interface position as functions of z and x, respectively. Differentiating (5.3) with respect to z gives the exact result [26]

$$\frac{\mathrm{d}x_i}{\mathrm{d}z} \left[u_i + p_s^{-1} \left(\frac{\partial u}{\partial z} \right)_i \right] + \int_0^{x_i} \mathrm{d}x \left(\frac{\partial u}{\partial z} + p_s^{-1} \frac{\partial^2 u}{\partial z^2} \right) - k \frac{\mathrm{d}x_i}{\mathrm{d}z} (u_i - 1) = 0. \tag{5.4}$$

Eq. (5.4) is the basis for the tail analysis carried out in this paper. It is equivalent to eq. (4.5), as shown in appendix B, which also discusses the more general case with $\beta \equiv D^s/D > 0$. Our strategy is to reexpress quantities involving the diffusion field in (5.4) in terms of quantities involving the interface shape. This generates an approximate differential equation for the interface shape. Below, we will use (5.4) to derive such an equation for the shape of the grooves of cellular patterns.

6. Tail approximation

Eq. (5.4) has terms involving the interface shape $x_i(z)$. This is a convenient representation for the interface shape deep in a groove since here the slope $dx_i/dz = \cot\theta$ (see fig. 5) is small. Using this fact and the narrowness of the groove will allow us to approximate eq. (5.4) for deep grooves. The method is very general and can be improved systematically. However, we expect the lowest order results given here to be sufficiently accurate to describe the groove region seen in many experiments.

The terms involving u_i in (5.4) can immediately be reexpressed in terms of the interface shape using the Gibbs–Thomson equation (4.6). Moreover, terms involving field derivatives like $(\partial u/\partial z)_i$ can also be approximated accurately by differentiating (4.8) since

$$u_i(z) \equiv u(x_i(z), z) = 1 - \frac{p_s}{\nu}\left[z + \pi^{-2}(\nu - 1)\kappa\right], \tag{6.1}$$

so that, by the chain rule,

$$\frac{du_i}{dz} = \left(\frac{\partial u}{\partial z}\right)_i + \left(\frac{\partial u}{\partial x}\right)_i \left(\frac{dx_i}{dz}\right) \tag{6.2}$$

$$= -\frac{p_s}{\nu}\left(1 - \frac{\nu - 1}{\pi^2}\frac{d\kappa}{dz}\right). \tag{6.3}$$

For small dx_i/dz we have from (6.2) that $(\partial u/\partial z)_i \approx du_i/dz$, and similarly, using also the narrowness of the grooves, $(\partial^2 u/\partial z^2)_i \approx d^2u_i/dz^2$. Finally, for narrow grooves we can approximate the terms under the integral in (5.4) by their values at the interface. In this way we find from (5.4) our basic groove equation [26]

$$\frac{dx_i}{dz}\left(\zeta - (1-k)p_s\pi^{-2}(\nu-1)\kappa - \pi^{-2}(\nu-1)\frac{d\kappa}{dz}\right) - x_i\pi^{-2}(\nu-1)\frac{d^2\kappa}{dz^2} - p_s x_i \pi^{-2}(\nu-1)\frac{d\kappa}{dz} = p_s x_i. \tag{6.4}$$

Here

$$\zeta = (\nu - 1) - (1 - k)p_s z \tag{6.5}$$

is the same quantity that evaluated at the tip in eq. (3.4) gives the LCS stability criterion. (Note that in (3.4), z_t was written in dimensional units.) For our purposes here, ζ gives information about the width of the planar two phase region $\Delta u_i(z)$, and can also be thought of as a dimensionless measure of vertical distance. As we will see, ζ appears repeatedly in the rest of this paper; this is why the ideas of LCS turn out to be of relevance to the matching theories. The tail equation (6.4) has also been derived independently by Mashaal et al. [29]

All the approximations leading to (6.4) can be improved systematically, but the lowest order result will prove sufficiently accurate for our purposes here. Deep in the grooves, terms involving the curvature become negligibly small and (6.4) reduces to

$$\zeta\, dx_i/dz = p_s x_i, \tag{6.6}$$

which has the solution

$$x_i(z) = A_0 \zeta^{-1/(1-k)}, \tag{6.7}$$

with A_0 an integration constant.

Thus as $\zeta \to \infty$ (i.e., $z \to -\infty$), grooves are predicted to close as a power law $x_i \sim |z|^{-t}$, where the exponent $t = 1/(1-k)$ depends only on k and is near unity for small k. This limiting result has been known for some time now, and is usually attributed to Scheil and Hunt [2,27,28].

For a real physical system with $\beta \equiv D^s/D$ small but non-zero, (6.7) must eventually become inaccurate sufficiently deep in the grooves because of the effects of diffusion in the solid ignored in the one-sided model. (Of course, our assumption of a linear phase diagram as in fig. 4 must also become inaccurate, e.g., at a eutectic point, but we do not analyze this possibility here.) In appendices B and C we discuss how the results of this section are modified when β is small but non-zero and derive an upper bound to the breakdown distance ζ_b beyond which (6.7) cannot be trusted. We also make some more general remarks about both the utility and the limitations of the predictions of the one-sided model.

Eq. (6.4) is much more general than the limiting Scheil result (6.7). The terms involving the curvature in (6.4) are essential to describe the transition region below the tip of a pattern where the nearly

vertical Scheil shapes must somehow "bend over" smoothly and join to tips with larger curvature. They also play a role near the closure region of finite depth grooves.

Eq. (6.4) is a nonlinear fourth order differential equation for the interface shape $x_i(z)$, as is easily seen by writing the curvature as

$$\kappa = -\left(\mathrm{d}^2 x_i/\mathrm{d}z^2\right)\left[1 + (\mathrm{d}x_i/\mathrm{d}z)^2\right]^{-3/2}. \qquad (6.8)$$

After requiring that all solutions reduce to (6.7) deep in the grooves as $\zeta \to \infty$, there are still two integration constants left free to vary [42]. Reasonable choices for these constants produce solutions that indeed bend over and resemble the beginnings of a cell tip [43]. It would be interesting to compare the solutions of (6.4) to experimental groove shapes, since we typically find that the limiting Scheil shapes are accurate only for rather large ζ.

In order to determine the integration constants explicitly, it is necessary to examine the region closer to the finger tip where the approximations leading to (6.7) become inaccurate. This occurs because the width of the groove increases and the slope $\mathrm{d}x_i/\mathrm{d}z$ becomes very large.

This cell tip region is the subject of the following sections 7 and 8. Once an accurate description of the tip region has been found, we still have the problem of combining the tip and tail approximations to obtain a globally acceptable solution. As shown in section 8, for a class of solutions with narrow grooves this can be carried out systematically by using the asymptotic matching procedure introduced by Dombre and Hakim [10].

7. Finite amplitude solutions and tip approximations

The derivation of our tail equation (6.4) was rather general, exploiting only the steepness and narrowness of the groove, and holds for all values of the partition coefficient k. However, in order to find an equation that holds in the tip region, we will further assume that k is small, which is the usual experimental limit. Small k produces an important simplification because there is a class of finite amplitude solutions (i.e., solutions without deep grooves) for which the diffusion field is nearly one dimensional, i.e., $u \approx u(z)$ only, even though the interface shape is far from planar. We can provide a simple treatment of such solutions. In the following, z_m represents the minimum value of z_i for these solutions.

7.1. The $k \to 0^+$ limit

It can be easily seen by direct substitution that in the limit $k \to 0^+$, the one-dimensional field

$$u(x, z) = u_B(z) = B_0\, \mathrm{e}^{-p_s z} \qquad (7.1)$$

provides an *exact* solution both for the diffusion equation (4.4) and the conservation condition (4.5), independent of the shape of the interface [44]. Given this asymptotic solution to the diffusion field, one can then integrate the Gibbs–Thomson equation (4.6) in the form

$$B_0\, \mathrm{e}^{-p_s z_i} = 1 - \frac{p_s}{\nu}\left[z_i + \pi^{-2}(\nu - 1)\kappa\right] \qquad (7.2)$$

to derive a variety of interface shapes consistent with this field and hence with all the DS steady state equations. Our goal is to explore this particular class of tip solutions for which $u(x, z)$ reduces to (7.1) in the limit $k \to 0^+$. To do so, we will first analyze the finite amplitude $k \to 0^+$ patterns given by eq. (7.2) and then discuss how these solutions are modified for k small but finite. The use of these solutions to construct the tip shape of cells with deep grooves is discussed in the next section.

Although the one-dimensional field satisfies both eq. (4.4) and eq. (4.5) in the limit $k \to 0^+$, in order that the solutions of (7.2) connect smoothly with those at small but finite k we need to impose an additional global conservation condition. The requirement that the *total* amount of impurities left behind in the solid is the same as the amount entering through the liquid implies for the one-sided model that all single-value interface shapes obey a simple and exact condition that is easily derived from the general flux equation (5.3). Evaluating (5.3) in the solid for $z < z_m$ and using (4.6), we have for any $k > 0$ (thus including the limit $k \to 0^+$)

$$\int_0^a z_i(x)\,\mathrm{d}x = -\pi^{-2}(\nu - 1)\int_0^a \kappa(x)\,\mathrm{d}x. \qquad (7.3)$$

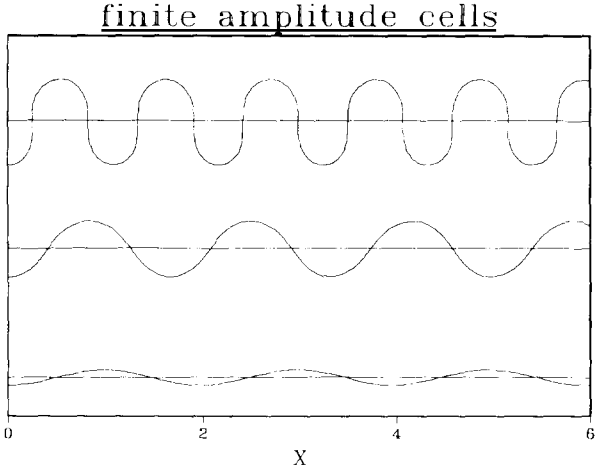

Fig. 6. Examples of finite amplitude solutions for $p_s = 0.15$ and $\nu = 1.5$. The horizontal lines indicate the location of the plane $z = 0$.

The latter integral can be evaluated exactly:

$$\int_0^a \kappa(x)\,\mathrm{d}x = \int_{s_m}^{s_t} \frac{\mathrm{d}\theta}{\mathrm{d}s}\frac{\mathrm{d}x}{\mathrm{d}s}\mathrm{d}s = -\int_{s_m}^{s_t} \frac{\mathrm{d}}{\mathrm{d}s}(\sin\theta)\,\mathrm{d}s$$

$$= \sin\theta_m - \sin\theta_t, \tag{7.4}$$

where we note from fig. 5 that $\mathrm{d}x/\mathrm{d}s = -\cos\theta$. Here s is the arc-length and we have used the fundamental definition $\kappa = \mathrm{d}\theta/\mathrm{d}s$. For the single-values cellular solutions like those in fig. 1a, $\theta_m = \theta_t = 0$, and (7.3) reduces to [45]

$$\int_0^a z_i(x)\,\mathrm{d}x = \int_{s_m}^{s_t} z_i(s)\frac{\mathrm{d}x}{\mathrm{d}s}\mathrm{d}s = 0, \tag{7.5a}$$

or

$$A(s_t) \equiv -\int_{s_m}^{s_t} z_i(s)\cos\theta\,\mathrm{d}s = 0. \tag{7.5b}$$

We will refer to this condition as the *equal area rule*, since it shows that for finite amplitude cells the areas above and below the line $z = 0$ are equal. See figs. 6 and 7 for examples. Note that with the sign conventions of fig. 5, $s_m > s_t$ in (7.5).

It is useful both conceptually and for practical numerical calculations to rewrite (7.2) as a system of first order equations parameterized by the arc-length s:

$$\frac{\mathrm{d}z}{\mathrm{d}s} = -\sin\theta, \tag{7.6}$$

$$\frac{\mathrm{d}x}{\mathrm{d}s} = -\cos\theta, \tag{7.7}$$

$$\frac{\mathrm{d}\theta}{\mathrm{d}s} = \frac{\pi^2}{\nu - 1}\left(\frac{\nu}{p_s}\left(1 - B_0\,\mathrm{e}^{-p_s z_i}\right) - z_i\right), \tag{7.8}$$

$$\frac{\mathrm{d}A}{\mathrm{d}s} = -z_i\cos\theta. \tag{7.9}$$

Eqs. (7.6) and (7.7) express exact geometric properties of a curve (see fig. 5) and (7.8) reexpresses the original equation (7.2). Finally, A in (7.9) is (7.5b) evaluated at an arbitrary upper limit s.

It is most convenient to think of solving these equations by an iterative process. First pick an initial guess for B_0. For fixed B_0, we can solve (7.6)–(7.9) as a simple initial value problem, starting at the minimum and integrating upward. By definition, the initial conditions are $x_m = 0$, $\theta_m = 0$ and $A_m = 0$ at the minimum, but we can pick any $z_m < 0$. We then integrate [46] forward to the tip (maximum) of the solution where again $\theta_t = 0$, and immediately find z_t, κ_t and $x_t \equiv a$. For fixed B_0, if z_m becomes too negative the solutions do not remain single-valued, and we reject them. Furthermore, even the single-valued solutions will in general not satisfy the equal area rule (7.5). Hence B_0

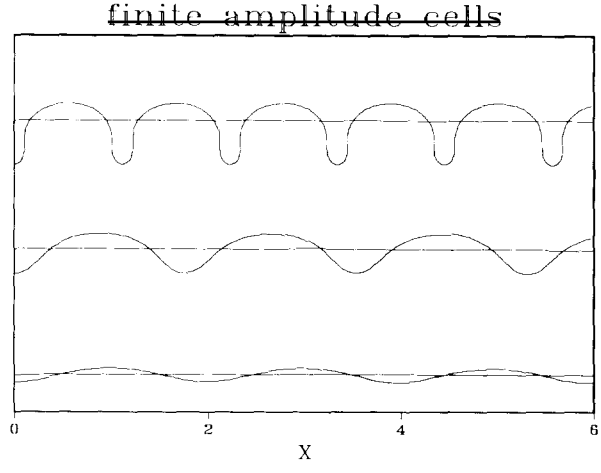

Fig. 7. Examples of finite amplitude solutions for $p_s = 4$ and $\nu = 1.5$.

must be varied and the integration process repeated until (7.5) is also satisfied. Thus, we can think of B_0 as being fixed by the global conservation requirement $A(s_t) = 0$. See figs. 6 and 7 for examples.

7.2. Finite amplitude shapes for $k \to 0^+$

As the discussion above demonstrates, eqs. (7.2) and (7.5) admit a *continuous family* of finite amplitude cellular solutions, whose half wavelength a is a continuous function of a single parameter [47] z_m. However, once these solutions have been found, properties of the family can be reexpressed in other terms, e.g., in terms of the dependence of the wavelength on the total amplitude, $z_t - z_m$, or on the curvature at the tip, κ_t. We now discuss these finite amplitude solutions in some detail. Figs. 6 and 7 shows some examples for fixed p_s and ν. Thus, the profiles in each figure are all members of the same family obtained by varying z_m. One immediately notices that the profiles shown in fig. 6 for $p_s = 0.15$ are almost symmetric. This is easy to understand since the equal area rule (7.5) shows that the average value of z_i vanishes. As a result, for small p_s, $B_0 \approx 1$ and the exponential factor $\exp(-p_s z)$ in (7.2) can be linearized, $\exp(-p_s z) \approx 1 - p_s z$. Since the equation for the shape of the resulting profiles then only contains terms odd in z, the profiles are reflection symmetric about the line $z = 0$. Clearly, for increasing p_s the nonlinear behavior of the exponential $\exp(-p_s z)$ becomes more important, and the bottom part of the finite amplitude cellular profiles narrows, as shown in fig. 7. This is illustrated quantitatively in fig. 8, where we plot the ratio w/a of finite amplitude cells whose maximum angle is 90°, as illustrated by the upper profiles in fig. 7. Here w is the width of the bottom region measured at the point where $\theta = \pm 90°$, so that for reflection symmetric cell shapes, $w/a = 1/2$. As fig. 8 shows, the ratio w/a becomes significantly smaller than $1/2$ only for Péclet number $p_s \gtrsim 1$, as expected. Moreover, by comparing the data points for profiles with (triangles, $\alpha_4 = 0.3$ in eq. (2.4)) and without (circles, $\alpha_4 = 0$) anisotropy, the ratio is essentially independent of the strength of fourfold crystalline anisotropy.

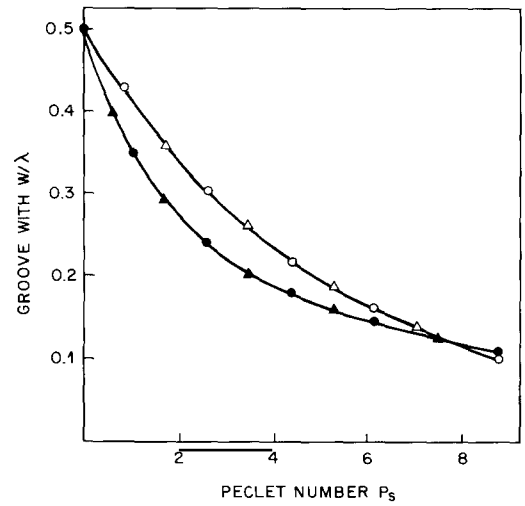

Fig. 8. Relative groove width w/a of cellular patterns with $\theta_{max} = \pm 90°$ for $\alpha_4 = 0$ (○, ●) and $\alpha_4 = 0.3$ (△, ▲). Solid symbols denote data for $\nu = 1.5$, open symbols data for $\nu = 4.5$.

It is also of interest to analyze the wavelength of these profiles. In the limit of small amplitude, we expect that the wavelength of these cellular shapes reduces to λ_s^0, the neutral stability wavelength in the $k \to 0^+$ limit given in eq. (4.3), since this represents a valid steady state solution of infinitesimal amplitude. It is easy to check that this is indeed the case: upon linearizing eqs. (7.2) and (7.5), we find that the solution is $z_i = C \cos \pi x$, $B_0 = 1$, and since our unit of length is $\lambda_s^0/2$, we see that the small amplitude wavelength indeed reduces to λ_s^0.

Figs. 6 and 7 already illustrate that the wavelengths of these cell profiles *decrease* with increasing amplitude, and fig. 9 shows that this is true both with and without crystalline anisotropy. These results therefore imply that for small k this particular branch of solutions lies *outside* the planar instability band. As discussed in the Introduction, we therefore expect these solutions in general to be unstable.

7.3. Results for k small but nonzero

In order to compare the previous $k \to 0^+$ results to cell shapes for realistic parameters, we now estimate the correction to this branch when k is small but finite. In the general case of a periodic

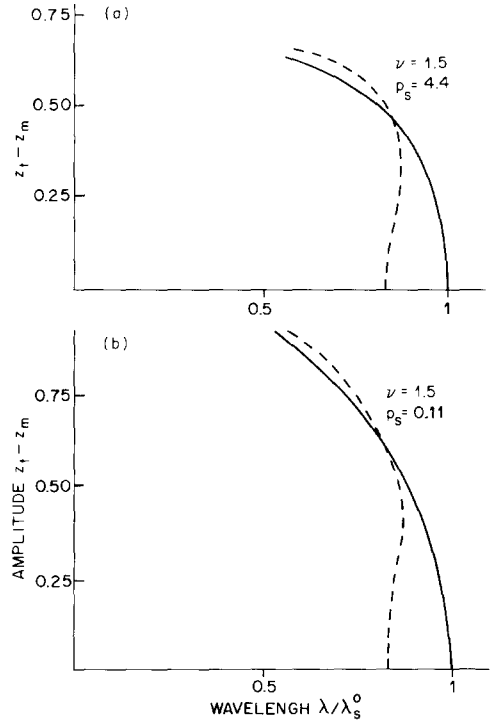

Fig. 9. Total amplitude $z_t - z_m$ versus wavelength λ/λ_s^0 of the family of cellular solutions given by eqs. (6.5)–(6.9) for two values of the Péclet number. The solid line corresponds to the case of isotropic surface tension and the dashed line of an anisotropic surface tension given by (2.4) with $\alpha_4 = 0.3$.

pattern, we can expand the diffusion field in the liquid ahead of a finite amplitude cellular solution in a Fourier series according to

$$u(x, z) = \sum_{n \geq 0} B_n \cos(q_n x)\, e^{-p_n(z - z_m)}, \tag{7.10}$$

where, in order that u satisfies the diffusion equation (4.4), the coefficients q_n and p_n are given by

$$q_n \equiv \pi n/a, \tag{7.11}$$

$$p_n \equiv \tfrac{1}{2}p_s + \tfrac{1}{2}\sqrt{p_s^2 + 4q_n^2}, \tag{7.12a}$$

$$p_0 = p_s. \tag{7.12b}$$

In appendix E, we show that the conservation boundary condition can be used to derive the following set of equations for the Fourier coefficients B_n,

$$\sum_{n \geq 0} M_{jn} B_n = N_j, \tag{7.13}$$

with

$$N_j \equiv k \int_0^a dx \cos(q_j x)\, e^{-(p_j - p_0)(z_i - z_m)}, \tag{7.14}$$

$$M_{jn} = \int_0^a dx \left[\cos(q_j x) \cos(q_n x)\, C_{nj} + q_n q_j \sin(q_j x) \sin(q_n x)\right] \times \frac{e^{-(p_j + p_n - p_0)(z_i - z_m)}}{p_0(p_n + p_j - p_0)}, \tag{7.15}$$

$$C_{nj} \equiv k p_0(p_n + p_j - p_0) + (p_n - p_0)(p_j - p_0). \tag{7.16}$$

We show in appendix E that eq. (7.13) for $j = 0$ is equivalent to the conservation condition (5.3) from which the equal area rule (7.5) was derived. Note also that although (7.13) has the form of a set of linear equations for the B_j's, the equations are really nonlinear, since both M and N depend on the interface profile $z_i(x)$, which in turn depends on the B_j's. Nevertheless, since all the N_j's are proportional to k, it is not surprising that the $k \to 0^+$ branch considered before has a regular k

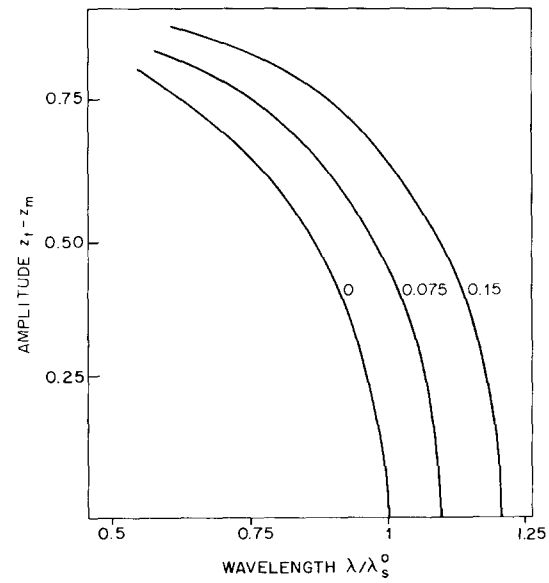

Fig. 10. Illustration of the k-dependence of the family of finite amplitude solutions whose $k \to 0^+$ limit is given by eqs. (6.5)–(6.9). Results shown are for $p = \sqrt{2}$, $\nu = 1.5$ and $k = 0$, 0.075 and 0.15.

expansion [48] with all B_j of $O(k)$ for $j \geq 1$. Indeed, we have checked this numerically in the case that eq. (7.13) is truncated to a few modes. This is easily done [49] by treating the variables B_j in much the same way as the variable B_0 was treated in the computer program described in section 7.2. Fig. 10 shows a representative example of an amplitude versus wavelength plot in the case $p_s = \sqrt{2}$, $\nu = 1.5$. The figure clearly illustrates that the k-dependence of this branch of solutions is rather smooth [50], and that the $k \to 0^+$ results remain fairly accurate for k small but nonzero, especially so for the large amplitude solutions that are important for the matching to cells with deep grooves. In fact, we already know from the work of Hakim et al. [10,29] that the k-dependence can be accounted for trivially in the $p_s \to 0$ limit through a reparametrization of the equation (see also ref. [31]). The present results show that the k-dependence of this branch of finite amplitude cellular solutions remains weak even for p_s of O(1).

7.4. Discussion

Although some of the shortcomings of the finite amplitude solutions analyzed in this section will reemerge later in the discussion of the matching analysis of cells with grooves, it is useful to mention some of them here. As we have seen the cellular shapes which can be obtained perturbatively in the limit $k \to 0^+$ (but p_s finite), all have wavelength λ smaller than λ_s. Thus, they lie outside the planar instability band, and we expect them to be *unstable*.

In a calculation for the symmetric model, Langer [51] found finite amplitude cellular solutions within the planar instability band. Although we do not find this kind of solution from our expansion, such finite amplitude solutions almost certainly exist in the one-sided model. The question of whether even the solutions within the planar instability band are *stable*, is, however, still a matter of debate. A few years ago, Caroli et al. [52] concluded that the Mullins–Sekerka instability in directional solidification corresponds to a subcritical (inverted) bifurcation for $k \lesssim 0.45$ and to a supercritical (forward) bifurcation for $k \gtrsim 0.45$. If the bifurcation is supercritical, one expects to find stable small amplitude cellular patterns very close to threshold, while if the bifurcation is subcritical such stable cells would not exist. Instead, just above threshold one expects the perturbation to evolve into large amplitude cell patterns, possibly cells with grooves. The picture of Caroli et al. [52] seems to be qualitatively consistent with most of the experimental observations, since small amplitude cells are normally seen [19] in liquid crystal ($k = O(1)$), while cells with grooves are found in most plastic crystals with k about 0.1–0.2. Nevertheless, both de Cheveigné et al. [6] and Trivedi [5] have seen apparently stable finite amplitude cells for materials with relatively small k values. Moreover, the conclusion of Caroli et al. [52] has recently been challenged [53] on theoretical grounds, and the issue appears to be unresolved at present. See section 10 for some remarks on this point.

8. Asymptotic matching of top and tail solutions

8.1. Inner and outer matching

We have not succeeded in finding a well-justified approximation that yields a single differential equation for the shape that is capable of accurately describing both the tip and tail regions of typical finger-like steady state DS patterns. However both in many experiments, and in the numerical studies of Ungar and Brown [4] the grooves remain narrow even near the tip. In this case, the work of Dombre and Hakim [10] suggests that there might be a "matching region" a distance of O(1) behind the tip where the narrow groove approximations leading to the "inner" equation (6.4) remain valid, while at the same time we are close enough to the tip that the "outer" equation (7.2) also is accurate. If this is the case, one can use the method of *asymptotic matching* to in effect join the tip and tail solutions, thus yielding a globally acceptable branch of solutions. As we will discuss in detail later, the small parameter ϵ in the matching scheme can be thought of as the width of the groove just below the matching region [54]. This important idea was first introduced by Dombre and Hakim [10] in their study of a

simplified model of DS with $k = 1$ and $p \to 0$. If differs from usual applications of asymptotic matching methods [30] in that the small parameter ϵ does not appear explicitly in the problem, but rather is determined self-consistently as a property of the matched solutions.

There have been many attempts [2,3,27] in the past to "patch" the Scheil solutions (6.7) to some smooth tip shape (say a semicircle), but the patching procedure was arbitrary, as was the form of the tip solution, and the results were rather sensitive to the particular patching method used. The use of (6.4), together with eq. (7.2) for the interface shape near the tip and method of asymptotic matching allows us to avoid these problems. As we shall see, however, the straightforward matching procedure yields a branch of cellular solutions with a ζ_t that is positive and finite, rather than cells that are close to the LCS criterion $\zeta_t \approx 0$.

Far below the matching region the curvature of the grooves as described by (6.4) is very small, while near the tip the curvature as given by (7.2) is O(1). The requirement that these different behaviors join smoothly in the matching region produces *consistency conditions* that are asymptotically exact in the limit of narrow grooves with $\epsilon \to 0$. These conditions in effect determine the boundary conditions needed to specify the solution of (7.2), which will now describe the tip of a finger consistent with deep grooves in the tails. This leads to a continuous family of fingerlike solutions, whose wavelength $2a$ is parametrized by the matching parameter ϵ. This behavior is analogous to that of the finite amplitude solutions discussed in section 7, where the wavelength is a function of a single parameter, e.g., the amplitude.

To begin the matching, let $z_m \equiv z_i^0(x = 0)$ where $z_i^0(x)$ is the (at present unknown) solution to the outer equation (7.2) that obeys the matching conditions derived below. In this section, the subscript m stands for "matching region" rather than for "minimum" as it did in section 7, but the idea is much the same. Now consider the inner equation (6.4). In the matching region near z_m, the solution $x_i(z)$ to (6.4) is by definition $O(\epsilon)$, and its curvature is small. Introducing the rescaled function $\tilde{x}_i$ by the relation

$$x_i \equiv \epsilon a \tilde{x}_i, \tag{8.1}$$

we look for a scaling of the variable z such that eq. (6.4) to lowest order in ϵ in the region near z_m can be written in parameter-free form. This determines the limiting scaling behavior of $x_i(z)$ and its derivatives as $\epsilon \to 0$. The only consistent scaling is

$$z - z_m = \left(\frac{\epsilon a(\nu - 1)}{\pi^2 \zeta_m} \right)^{1/3} \tilde{z}, \tag{8.2}$$

where ζ_m is given by (6.5) evaluated at z_m. Note that since we want ϵ to be the only small length scale in the problem, we have to assume that ζ_m is positive and finite. Eq. (6.4) to lowest order (at $O(\epsilon)^{2/3}$) thus becomes

$$\frac{d\tilde{x}_i}{d\tilde{z}} \left(1 - \frac{d^3\tilde{x}_i}{d\tilde{z}^3} \right) = \tilde{x}_i \frac{d^4\tilde{x}_i}{d\tilde{z}^4}, \tag{8.3}$$

or

$$\frac{d}{d\tilde{z}} \left[\tilde{x}_i \left(1 - \frac{d^3\tilde{x}_i}{d\tilde{z}^3} \right) \right] = 0. \tag{8.4}$$

Corrections to (8.3) are higher order in ϵ and thus vanish as $\epsilon \to 0$. Note that $\tilde{z}$ is a "rapid" variable in that a fixed (unscaled) distance Δz above (or below) z_m implies that $\tilde{z} \to \infty$ (or $-\infty$) as $\epsilon \to 0$. A first integral of (8.4) is

$$\frac{d^3\tilde{x}_i}{d\tilde{z}^3} = 1 - \frac{1}{\tilde{x}}, \tag{8.5}$$

where the integration constant was fixed by requiring $\tilde{x}_i \to 1$ as $\tilde{z} \to -\infty$ where $d^3\tilde{x}/d\tilde{z}^3 \to 0$, so that in unscaled variables the width of the groove is ϵa just below the matching region. (Thus ϵ is the relative width of the groove in this region.) Eq. (8.5) is identical to that found by Dombre and Hakim [10].

We now examine the behavior of (8.5) as $\tilde{z} \to \infty$. In unscaled distances, this probes the region just above z_m where the curvature terms in (8.4) first become important. This is the critical region that allows a smooth joining of tip and tail solutions.

It is clear from (8.5) that $\tilde{x}_i$ diverges like $\tilde{z}^3/6$ as $\tilde{z} \to \infty$. Direct substitution gives the leading behavior in this limit

$$\tilde{x}_i(\tilde{z}) = \tilde{z}^3/6 + \beta\tilde{z}^2/2 + \gamma\tilde{z} + \delta - 3\ln(\tilde{z}) + O(\tilde{z}^{-1}). \tag{8.6}$$

Note that the coefficient of the logarithmic term in (8.6) is determined by the requirement that it balance the highest order correction due to the $\tilde{x}_i^{-1}$ term on the right-hand side of (8.5). The coefficients β, γ, and δ of the other terms in (8.6) can be determined numerically by integrating (8.5). Each of these constants depends on the choice of origin of (i.e., on z_m), but translationally invariant combinations can be determined by considering the changes in each coefficient induced by an infinitesimal translation $\tilde{z} \to \tilde{z} + \Delta\tilde{z}$ in (8.6). This yields

$$\Delta\tilde{x}_i(\tilde{z}) \equiv \tilde{x}_i(\tilde{z} + \Delta\tilde{z}) - \tilde{x}(\tilde{z}) = \Delta\tilde{z}(\tilde{z}^2/2 + \beta\tilde{z} + \gamma - 3/\tilde{z} + \ldots). \quad (8.7)$$

Thus changes in the coefficients in (8.6) due to this translation are

$$d\beta = \Delta\tilde{z}, \quad (8.8a)$$

$$d\gamma = \beta\Delta\tilde{z}, \quad (8.8b)$$

$$d\delta = \gamma\Delta\tilde{z}. \quad (8.8c)$$

From (8.8a) and (8.8b) we have $d\gamma/d\beta = \beta$, or

$$\beta^2 - 2\gamma = C_1, \quad (8.9)$$

where C_1 is a constant that must be determined numerically from (8.6). Similarly from (8.8a), (8.8c), and (8.9) we have

$$\delta - \tfrac{1}{3}\beta(\gamma - C_1) = C_2, \quad (8.10)$$

where C_2 is another constant. Thus we have two relations involving the three quantities β, γ, and δ that are independent of the choice of origin. These invariant combinations can be determined more accurately from a numerical integration of (8.5) than can the individual values of β, γ, and δ. To carry out the matching procedure to lowest order it turns out that we need only determine C_1. We find numerically that [55] $C_1 = -6.38 \pm 0.02$.

The basic idea of the asymptotic matching method is to match the large $\tilde{z}$ asymptotics of the inner solution $\tilde{x}_i(\tilde{z})$ in (8.6) to the Taylor series expansion of the outer (tip) solution about $z = z_m$, when expressed as a function of z. We write this outer solution as $x_i^0(z)$. This is an example of the asymptotic matching principle discussed by Van Dyke [30], where boundary conditions for the outer solution are fixed by the requirement that the inner expansion of the outer solution equals the outer expansion of the inner solution. Letting θ_m and κ_m be the angle and curvature of the desired solution to (7.2) at z_m (i.e., at $x = 0$), then we have by exact geometric properties of a curve (see fig. 5):

$$\frac{dx_i^0}{dz_m} = \cot\,\theta_m, \quad (8.11)$$

$$\frac{d^2x_i^0}{dz_m^2} = \kappa_m/\sin^3\theta, \quad (8.12)$$

$$\frac{d^3x_i^0}{dz_m^3} = \frac{3\kappa_m^2\cos\theta_m}{\sin^5\theta_m} + \frac{1}{\sin^3\theta_m}\frac{d\kappa}{dz_m}. \quad (8.13)$$

Eqs. (8.12) and (8.13) follow from differentiating the definition (8.11). Eqs. (8.11)–(8.13) give the first few coefficients b_n in the Taylor series expansion about z_m of the outer solution:

$$x_i^0(z) = \sum_n b_n(z - z_m)^n/n!. \quad (8.14)$$

To carry out the matching [10,26,29], we rewrite (8.14) in *inner* variables, using (8.1) and (8.2):

$$\tilde{x}_i^0(\tilde{z}) \equiv x_i^0(z)/\epsilon a = \sum_n \tilde{b}_n\tilde{z}^n/n!, \quad (8.15)$$

and then directly identify the $\tilde{b}_n$ with the coefficients from the inner solution (8.6). We find from (8.14) and (8.15) that

$$\tilde{b}_n = \frac{b_n}{\epsilon a}\left(\frac{\epsilon a(\nu - 1)}{\pi^2\zeta_m}\right)^{n/3}, \quad (8.16)$$

and that to lowest order as $\epsilon \to 0$, the contributions from powers $n > 3$ in (8.14) vanish when expressed in inner variables as in (8.15).

Comparing the linear term ($n = 1$) in (8.15) (see (8.11)) to that in (8.6), we see that cot θ_m is very small, of $O(\epsilon^{2/3})$, as $\epsilon \to 0$, i.e., that θ_m is close to $\pi/2$. This is physically very reasonable in order to match onto the nearly vertical solution of the inner equation (6.4) in this limit.

The matching for $n = 2$ implies to lowest order that $\kappa_m = \beta(\epsilon a)^{1/3}\ [\zeta_m\pi^2/(\nu - 1)]^{2/3}$. As one would expect for matching to the narrow grooves, this shows that the curvature in the matching

region also has to be small. The value of β is not fixed at this order, however. The discussion after eqs. (8.8) shows that a change in the value of β corresponds to a vertical translation of the inner (groove) profile by an amount of order unity in the inner variable, i.e. by a distance of order $\epsilon^{1/3}$. At this order of the matching, this distance is not determined [56], and we are free to take $\beta = 0$ so that

$$\kappa_m = 0. \tag{8.17}$$

Using $\beta = 0$ in (8.9) then fixes $\gamma = \gamma^* = 3.19 \pm 0.02$ from our numerical determination of C_1. Carring out the matching of the linear $n = 1$ terms then yields

$$\cot\,\theta_m = \gamma^* (\epsilon a)^{2/3} \left(\frac{\pi^2 \zeta_m}{\nu - 1} \right)^{1/3} \tag{8.18}$$

for the $n = 1$ matching condition. Thus $\pi/2 - \theta_m$ is indeed very small for $\epsilon \to 0$, as previously mentioned.

As we have stressed before, our narrow groove results are valid for any k. Therefore, the matching conditions (8.17) and (8.18) would also be the proper boundary conditions if we would have an expression for the outer (tip) shape at arbitrary k. The status of the matching for $n = 3$ is slightly different, however. From (8.13), (8.15) and (8.16), we get to lowest order in ϵ the matching condition

$$\frac{d\kappa}{dz_m} = \frac{\pi^2 \zeta_m}{\nu - 1}. \tag{8.19}$$

The curvature appearing here on the left hand side is the curvature of the outer profile. Upon expanding this as $\kappa = \kappa^0 + k\kappa^1 + O(k^2)$ with κ^0 as given by (7.2), and using the definition of ζ given in (6.5), this condition can be written in the form

$$-p_s \kappa_m^0 + k \frac{d\kappa^1}{dz_m} + O(k^2) = \frac{\pi^2 k p_s z_m}{\nu - 1}. \tag{8.20}$$

This result clearly shows that this matching condition involves higher order terms in the k-expansion of the outer profile as well. Note, however, that in the limit $k \to 0^+$, eq. (8.20) is consistent with the condition (8.17) found above. Moreover, we do not need to use eq. (8.20), since as we have seen in section 7, the outer boundary conditions (8.17) and (8.18) are sufficient to integrate the tip equations (7.6)–(7.8) for a given constant B_0.

8.2. Conservation requirements

With (8.17) and (8.18) as initial conditions, we can integrate the outer equations (7.6)–(7.8) that describe the fingertip region, using the same program as before in section 7. For fixed B_0 in (8.8), the condition $\kappa_m = 0$ in (8.17) fixes z_m, and (8.18) gives [57] the initial angle θ_m. We can now integrate (7.6)–(7.8) to the tip, determined by the condition $\theta_t = 0$, and read off the dimensionless wavelength $2a$.

Just as was the case for the finite amplitude solutions discussed in section 7, the appropriate value of B_0 is determined by a global conservation requirement. In this case of cells with grooves, we use the fundamental conservation condition (5.3), applied to a line in the matching region. Making the usual narrow groove approximations, still valid in the matching region, we have from (5.3)

$$x_m \left(u_m + p_s^{-1} \frac{du_m}{dz} \right) = \frac{k p_s}{\nu} \int_{x_m}^{a} dx \left(z_i(x) + \frac{\nu - 1}{\pi^2} \kappa(x) \right). \tag{8.21}$$

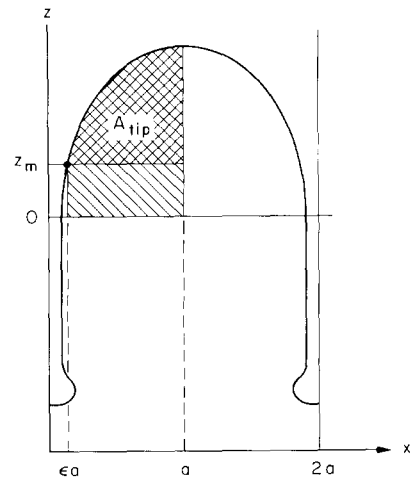

Fig. 11. Illustration of the area A_0 and A_{tip} used in eqs. (8.24)–(8.26). A_{tip} is the cross-hatched area and A_0 is the sum of the two hatched areas.

Here $x_m = x_i(z_m)$ and $u_m = u_i(z_m)$. We evaluate to lowest order in ϵ the left hand side of (8.21) using the inner solution and the right hand using the outer solution.

The first term on the right then gives A_0, the net area bounded by the tip profile, and the lines $x = \epsilon a$ and $x = a$, measured relative to the line $z = 0$. See fig. 11. The second term, as in (7.4), yields $\pi^{-2}(\nu - 1)\sin\theta_m$.

To evaluate the left hand side in the matching region we note that to lowest order

$$x_m\left(u_m + p_s^{-1}\frac{du_m}{dz}\right) = \nu^{-1}x_m\left(\nu - 1 - p_s\left[z + \pi^{-2}(\nu-1)\kappa\right] - \pi^{-2}(\nu-1)\frac{d\kappa}{dz}\right) \tag{8.22}$$

$$\approx \nu^{-1}x_m\left(\zeta - (\nu-1)\pi^{-2}\frac{d^3x_i}{dz^3} - p_s k z\right)_m, \tag{8.23}$$

since $\kappa_m \approx 0$ in the matching region. Using (8.5) rewritten in unscaled variables, the right-hand side of (8.23) reduces to $\nu^{-1}\epsilon a(\zeta_m - p_s k z_m)$.

With these approximations, the conservation requirement (8.21) can be written as

$$A_0 = -\pi^{-2}(\nu-1)\sin\theta_m + \frac{\epsilon a(\zeta_m - p_s k z_m)}{p_s k}. \tag{8.24}$$

The condition (8.24) then determines the appropriate value for B_0 in (7.8).

We note that an analysis similar in spirit to the one given here has been given independently by Mashaal et al. [29] in the limit $p \to 0$. However, they arrive at their result analogous to (8.24) by assuming an infinitely deep groove and using the Scheil shape to integrate the groove area [58]. In this approach, the ϵ/k behavior of the rightmost term in (8.24) reflects the fact that the area of the grooves diverges as $1/k$ for $k \to 0^+$ due to the asymptotic Scheil behavior (6.7). Our derivation above relies only on the validity of the inner equation (6.4) in the *matching region*, and therefore shows more clearly that (8.24) holds both for cells with infinite grooves [59] and for cells with finite depth but narrow grooves. As before, however, the analysis is only valid as long as ζ_m remains positive.

The conservation condition (8.24) can be used to obtain a simple estimate for the position z_m or the parameter ζ_m. To see this, note that to the relevant order in ϵ, $\sin\theta_m = 1$, and that $A_0 = a(1-\epsilon)z_m + A_{tip}$, where A_{tip} is the area above the matching line (the cross-hatched region of fig. 11). To get an order of magnitude estimate, assume the tip is a semicircle. We then find

$$A_{tip} \approx \pi a^2/4. \tag{8.25}$$

In general, with $A_0 = a(1-\epsilon)z_m + A_{tip}$ and the definition (6.5) of ζ_m, we get from (8.24) for the vertical position z_m the result

$$\frac{p_s z_m}{\nu - 1} = \frac{1}{k + (1-k)\epsilon} \times\left(\epsilon - \frac{p_s k}{(\nu-1)a}\left[A_{tip} + \pi^{-2}(\nu-1)\right]\right). \tag{8.26}$$

Thus, for $\epsilon = 0$, z_m is always negative. However, for increasing ϵ, z_m rapidly increases, since

$$\left.\frac{dz_m}{d\epsilon}\right|_{\epsilon=0} = \frac{1}{kp_s}\left(\nu - 1 + \frac{p_s(1-k)}{a} \times\left[A_{tip} + \pi^{-2}(\nu-1)\right]\right). \tag{8.27}$$

The significance of these results is the following. As we have seen earlier in this section, for the matching method to be consistent, ζ_m needs to be positive and finite. We see that this is indeed the case for the branch of solutions considered here, since (8.26) can be rewritten as

$$\zeta_m = \frac{\nu - 1}{1 + (1-k)\epsilon/k} \times\left(1 + \frac{p_s}{(\nu-1)a}\left[A_{tip} + \pi^{-2}(\nu-1)\right]\right). \tag{8.28}$$

Thus, according to this lowest order estimate for z_m as a function of ϵ, ζ_m is positive and O(1) for

small $\epsilon \lesssim k$, and so the matched asymptotic expansion is indeed self-consistent.

At the same time, however, (8.28) illustrates the problems associated with the branch of solutions that can be analyzed with the matching method, assuming only a single matching region exists. The results to lowest order in ϵ suggest that it leads to a branch of solutions that is incompatible with the $\zeta_t \approx 0$ behavior that we expect for physically relevant solutions on the basis of the LCS criterion. Apparently, this method can only be used consistently to probe a physically irrelevant branch of solutions.

This conclusion is forced upon us even more strongly in the small Péclet number limit. For $p_s \to 0$, Mashaal et al. [29] and Karma and Pelcé [31] have found that the lowest order estimate (8.26) remains accurate for the Saffman–Taylor-like branch over the whole interval $0 < \epsilon < 1/2$. Moreover, in this limit, we can take $\zeta_t \approx \zeta_m$ and neglect the second term between square brackets in (8.28). This equation then shows, however, that $\zeta_t \approx \zeta_m$ can only be made small (for $\nu - 1 = O(1)$) by taking ϵ/k large. For realistic values of k and $\nu - 1$ of O(1), only cells with wide grooves ($\epsilon \gg k$) can be reasonably close to the LCS criterion $\zeta_t \approx 0$. In section 10, we will compare this prediction in more detail with the LCS criterion and with the experimental measurements.

9. Cells with grooves: results

The discussion in the last section shows that the solutions for the cell shapes with grooves can be obtained by integrating the same finite amplitude equations as described in section 7, but with the boundary conditions (8.17), (8.18) and (8.24) instead of the ones used there. In the case of the finite amplitude cellular solutions, a unique solution was found for some particular choice of the minimum z_m and a given set of experimental parameters. However, the value of z_m was not prescribed by the equations, and so a family of solutions was obtained. Here, again, the boundary conditions (8.17), (8.18) and (8.24) completely determine the solution for fixed p, ν *and* ϵ. However, ϵ is only a parameter that characterizes the solution in the matching region. SInce ϵ is not fixed, we again obtain a one-parameter family of periodic fingerlike cellular solutions, in this case parameterized by ϵ.

The simplest test of the theory is given by a comparison of experimental and theoretical cellular wavelengths in a diagram like fig. 3. Both for ease of comparison in such a diagram and with other approaches where the half wavelength $\lambda/2$ is taken as unit of length [21,26], and because this ratio plays an important role in the small Péclet number limit [10,29,31], we will denote the quantity $(\pi a)^{-2}$ by σ:

$$\sigma \equiv \left(\frac{1}{\pi a}\right)^2 = \left(\frac{\lambda_s^0}{\pi \lambda}\right)^2, \tag{9.1a}$$

$$= \frac{4\nu d_0 l_D}{\lambda^2(\nu - 1)}. \tag{9.1b}$$

In view of the form (9.1b), σ can be thought of as a dimensionless surface tension parameter, but we will stress here [60] its fundamental importance as a ratio measuring the (dimensional) wavelength of a periodic cell pattern relative to the neutral stability length λ_s^0.

We now discuss our results for cells with deep grooves like those of figs. 2 and 1b. Fig. 12 shows the typical behavior of σ as a function of the relative groove width ϵ for several values of the parameters. The maximum value of σ is of order unity and σ increases with increasing Péclet number. This implies that the minimum cell wavelength for cells with narrow grooves as $\epsilon \to 0$ is of order $\lambda_s^0/3$ or smaller. Thus, as indicated by the dashed line in fig. 3, the minimum cell width of the branch calculated perturbatively always lies well outside the planar instability band. This is true for essentially all parameters.

This result could of course already have been anticipated from the results described in section 7: the finite amplitude solutions whose maximum angle is around 90° have a wavelength roughly a factor 2 smaller than λ_s^0. Since we use only part of these finite amplitude solutions to match to the groove shapes, the minimum wavelength of cells with grooves is again smaller by about another factor of 2, hence $\sigma_{max} \gtrsim 1$.

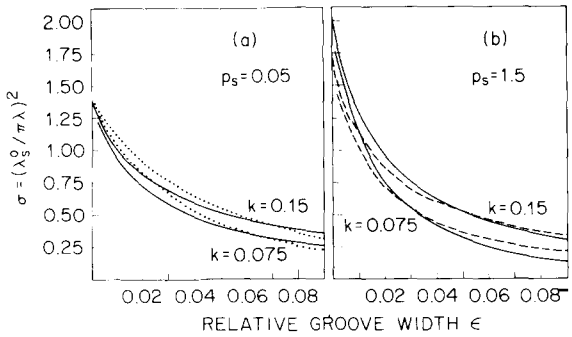

Fig. 12. The ratio $\sigma \equiv (\lambda_s^0/\pi\lambda)^2$ as a function of the relative groove width ϵ. (a) Results for $p_s = 0.05$ and $k = 0.075$ and $k = 0.15$ (full lines). The dotted lines indicate the results based on the $p \to 0$ mapping onto viscous fingering for these two values of k, obtained with the aid of the interpolation formula (10.5). In the $p \to 0$ limit, the σ versus ϵ curves have no ν dependence, as can be seen from (10.11). Note that our results based on the first nontrivial term in the ϵ expansion follow the exact results quite well throughout the range $0 \le \epsilon < 0.09$. (b) For $p_s = 1.5$ and $\nu = 1.5$ (full line) and $\nu = 4$ (dashed line) for the same two values of k as in (a). Figs. (a) and (b) illustrate that for small ϵ, σ increases with p_s.

Cells with wider grooves (larger ϵ) have a larger wavelength, since σ is a decreasing function of ϵ. For this reason, we have schematically indicated the ϵ expansion in fig. 3 by the arrows in the direction of increasing cell wavelength.

Fig. 12 shows that as k becomes smaller, the ratio σ decreases faster as a function of ϵ. This is mainly a result of the ϵ/k term in the conservation condition (8.24). However, for small but realistic values of k, say $k \approx 0.1$–0.2, σ remains substantially larger than $1/\pi^2 \approx 0.1$ over the range of ϵ values where the first term in the matched asymptotic expansion used here can be considered accurate. In other words, for realistic values of the parameters, our expansion results are only accurate over a range of wavelengths roughly of the size of the arrows in fig. 3. Since they do not extent into the planar instability band, we expect the cell patterns computed here to be unstable (see section 1). As mentioned earlier, we in fact believe that all solutions of this branch are unstable, even those that lie within the planar instability band, since their value of ζ_t is always positive and never close to the LCS value $\zeta_t \approx 0$.

In the above, we used small but realistic values of k, even though our outer (tip) profiles were computed with the simple exponential profile (7.2), which is exact only in the $k \to 0^+$ limit. Nevertheless, the results for the k dependence of the branch of finite amplitude solutions reported in fig. 9 indicate that the small k corrections to the tip profile will not change our conclusion drastically. We have verified this explicitly by taking higher Fourier modes into account as described earlier in section 7.3. We have also analyzed the effect of a cubic anisotropy (2.4) in the surface tension. As one might have anticipated from figs. 8 and 9, the presence of anisotropy does not change the above results qualitatively for $\alpha_4 \lesssim 0.3$.

10. General implications of results and comparison with the LCS criterion

We now wish to show that the above results have a number of important implications that warrant further theoretical and experimental study.

The ratio σ introduced in (9.1) measures the wavelength of the periodic cell pattern relative to λ_s^0 defined in (4.3), which under most circumstances is a good measure of the neutral stability wavelength. The narrow grooved patterns we have calculated perturbatively all have values of σ of order unity.

On the other hand, as mentioned already in the Introduction, in experiments one usually observes wavelengths that are about an order of magnitude larger than the minimum cell wavelength indicated by a dashed line in fig. 3. Thus, typical experimental cells have $\sigma \lesssim 10^{-2}$. For example, for the data of the Cheveigné et al. [8] shown in fig. 3 one finds [61,62]

$$0.3 \lesssim p \lesssim 1.2, \quad \sigma \approx 6 \times 10^{-3}. \tag{10.1}$$

Moreover, these and other experimentally observed cells typically seem to have *narrow* grooves (we estimate $\epsilon \approx 0.13$ for the cell shapes shown in fig. IV.11 of Kurowski [63]) but with small σ. However, *all* the analytical results based on asymptotic matching using a single matching region – those found by us as well as those based

[29,31] on the $p \to 0$ mapping onto viscous fingering – predict that small σ cellular shapes should have *wide* grooves, with $\epsilon \gtrsim 0.4$. We believe this is a serious discrepancy.

Of course, direct comparison with experiment is generally hampered by the fact that the theory does not take into account effects relating to the cell shape in the third dimension. However, Misbah et al. [64] have shown numerically that without adjustable parameters, the two-dimensional one-sided model used herein does have narrow grooved solutions that fit the experimental shapes of de Cheveigné et al. [8] very well. It would be interesting to check numerically whether this agreement between the theoretical model and experiment continues to hold at small p. These small σ solutions with narrow grooves are incompatible with the perturbative results obtained here for the same model.

We can analyze this question in more detail for the case of the mapping onto viscous fingering. Let us first recall that the steady state equations describing Saffman–Taylor (ST) fingering [10,11] can be written as

$$\nabla^2 \phi^{\mathrm{ST}} = 0, \tag{10.2}$$

$$\left(\hat{n} \cdot \nabla \phi^{\mathrm{ST}}\right)_t = \cos\theta, \tag{10.3}$$

$$\phi_t^{\mathrm{ST}} = \sigma^{\mathrm{ST}} \kappa, \tag{10.4}$$

where $\phi^{\mathrm{ST}} = -b^2(P - P_0)/(12\mu V W)$ and $\sigma^{\mathrm{ST}} = b^2\gamma/12\mu V W^2$. Here b is the plate spacing, μ the viscosity, V the finger velocity, P the pressure field, P_0 the pressure inside the finger, γ the surface tension, and W the cell half width (taken as the unit of length).

Using the matching method on which our analysis in this paper is based, Dombre and Hakim [10] show that for "fat" viscous fingers whose width approaches the cell width $2W$, σ^{ST} as defined here [65] approaches the maximum value 1.393. They also derive the limiting behavior for small ϵ of $\sigma^{\mathrm{ST}}(\epsilon)$, where ϵ is the relative groove width at the base of the finger. One finds that viscous fingers with narrow grooves are associated with values of σ^{ST} of order unity, and that $\epsilon \to 1/2$ in the small surface tension limit where $\sigma^{\mathrm{ST}} \to 0$, so that the maximum groove width is $1/2$. Karma and Pelcé [31] give a convenient interpolation formula fitting numerical results for $\epsilon \lesssim 0.4$, which can be written as

$$\sigma^{\mathrm{ST}} \approx \frac{1.393(1 - 2\epsilon)}{1 + 15.7\epsilon}. \tag{10.5}$$

Returning now to the DS problem, the analogy to viscous fingering can be seen most easily if we temporarily use the half wavelength of the cells as the unit of length and introduce a modified field [10,29] ϕ by the equation

$$u = 1 - p(z + \phi)/\nu, \tag{10.6a}$$

or

$$\phi = \frac{\nu}{p}\left(1 - \frac{p}{\nu} z - u\right). \tag{10.6b}$$

The field ϕ measures the difference between the impurity concentration field u and its dominant variation in the z-direction along a gently curved piece of the interface as indicated by the phase diagram. Substituting ϕ into eqs. (4.4)–(4.6), we find exactly the modified DS equations

$$\nabla^2 \phi + p\, \partial\phi/\partial z = -p, \tag{10.7}$$

$$\left[\zeta_t - (1 - k)p(\nu - 1)\sigma\kappa\right] \cos\theta = (\hat{n} \cdot \nabla\phi)_t, \tag{10.8}$$

$$\phi_t = (\nu - 1)\sigma\kappa. \tag{10.9}$$

Here $\zeta_t \equiv (\nu - 1) - (1 - k)pz_t$ is the usual LCS parameter (3.4) evaluated at a general position z_t measured in units of the half wavelength.

These equations are valid for any p, but we now take the limit $p \to 0$ in the following natural way [29]. We examine the region near the tips, allowing for the possibility that pz_t reaches a finite limit as $p \to 0$, but make the important assumption, to be verified later, that ζ_t remains greater than zero. In the fingertip region, of O(1) in our present units, we can then ignore the z-variation of ζ_t in (10.8), replacing it by ζ_t. Then ignoring all other terms proportional to p, we see the modified DS equations become identical in form to the ST equations given above if we let $\phi/\zeta_t = \phi^{\mathrm{ST}}$ and

$$\frac{(\nu - 1)\sigma(p \to 0)}{\zeta_t(p \to 0)} = \sigma^{\mathrm{ST}}. \tag{10.10}$$

As discussed in section 8, for the branch of solutions calculated from a matching analysis, ζ_m is given by (8.28), where we now ignore terms proportional to p. Although this result was derived here to lowest order in ϵ only, Mashaal et al. [29] and Karma and Pelcé [31] show that in the small Péclet number limit, this result is actually accurate for all $0 \le \epsilon \le 1/2$. Since for $p \to 0$ we can take $\zeta_m \approx \zeta_t$, (8.28) and (10.10) therefore give

$$\frac{\sigma(p \to 0)}{\sigma^{ST}} = \frac{\zeta_t(p \to 0)}{\nu - 1} = \frac{1}{1 + (1-k)\epsilon/k}. \tag{10.11}$$

As we saw above, in the derivation of the mapping of cellular profiles onto viscous finger shapes, one explicitly assumes that ζ_t remains finite. According to (10.11), this is indeed the case. Therefore, this mapping *does* indeed yield a self-consistent branch of cellular shapes for the DS problem in the limit $p \to 0$. We refer to this as the ST branch of solutions. At the same time, however, (10.11) unambiguously shows that, except for unrealistically small values of k, these solutions are never close to the LCS criterion $\zeta_t \approx 0$, and that such solutions with small σ correspond to fingerlike shapes with small σ^{ST}, and hence from (10.5) to shapes with wide grooves. For example, cellular shapes in this branch with $\sigma \lesssim 10^{-2}$ have a relative groove width $\epsilon \gtrsim 0.4$ for almost all values of k. Cells with such wide grooves are rarely seen in experiments, not even in those of Trivedi and coworkers [66] at Péclet numbers as small as 0.02. (However, it is possible that effects relating to the third dimension could modify the apparent groove width.)

This discrepancy can not be attributed to finite p corrections of the above results, since the calculations presented in this paper for the extension of this same branch to k small but p of O(1) show that these are relatively small. Numerical calculations by Ben-Amar and Moussallam [67] for general values of p and $k = 1$ agree with this conclusion. Fig. 12 shows that the p dependence of σ is small. That the p-dependence of ζ_t for this branch is small can be seen from the following. In order to obtain ζ_t from our earlier results for ζ_m, we neglect the term $(\nu - 1)/\pi^2$ in (8.26) and use the approximation (8.25), $A_{tip} \approx \pi a^2/4 \approx a^2$. We can then write (8.26) for the dimensional matching position z_m as

$$\frac{z_m(p)}{l_T} \lesssim \frac{\epsilon(1-\nu^{-1})}{k + (1-k)\epsilon} - \frac{\lambda}{2l_T} = \frac{z_t(p \to 0)}{l_T} - \frac{\lambda}{2l_T}. \tag{10.12}$$

Here, the inequality sign arises both from the fact that we have neglected the $(\nu - 1)/\pi^2$ term and that we have used $k/[k + (1-k)\epsilon] < 1$. Since $z_t \approx z_m + \lambda/2$, we can rewrite (10.12) as

$$\frac{z_t(p)}{l_T} \lesssim \frac{z_t(p \to 0)}{l_T} = \frac{\epsilon(1-\nu^{-1})}{k + (1-k)\epsilon}, \tag{10.13a}$$

$$\zeta_t(p) \gtrsim \zeta_t(p \to 0) = \frac{\nu - 1}{1 + (1-k)\epsilon/k}. \tag{10.13b}$$

It is important to realize that the above analysis of the ST branch and the extension thereof to $p = O(1)$ is based on the (implicit) assumption that there is just one small parameter, the groove width ϵ, and that ϵ can be taken arbitrarily small. With this assumption, a simple scaling can be performed in the matching region for $\epsilon \to 0$. It is quite possible that other branches of cells with narrow grooves exist that cannot be analyzed in terms of this simple scaling. As the discussion of eqs. (10.7)–(10.9) for small p shows, the assumption of a single small parameter ϵ breaks down in particular for solutions for which ζ is very small, as one might expect to happen on the basis of the LCS criterion. We have not attempted to extend the analysis of (6.4) to this case, since we have no proper tip profiles with wavelengths in the planar instability band to match these solutions to.

Since the quantities z_t and ζ_t can be obtained directly from temperature measurements at the tip [40], they are in fact much easier to compare with experimental data or theoretical predictions such as the LCS prediction $\zeta_t \approx 0$ than are predictions involving the groove width ϵ. In fig. 13 we plot z_t/l_T as a function of ν for $k = 0.1$, the value quoted for the succinonitrile–acetone mixture studied by Esaka and Kurz [40]. (As in (10.13), z_t is here the dimensional tip position.) The dashed line in this figure indicates the line $\zeta_t = 0$ corre-

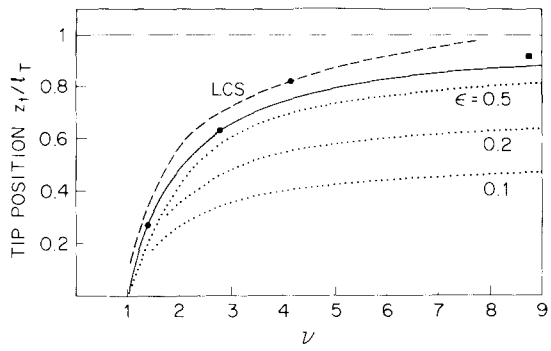

Fig. 13. Plot of the tip position z_t/l_T versus ν. The dashed line corresponds to the LCS line given by $\zeta_t = 0$ or $z_t/l_T = (1 - 1/\nu)/(1-k)$ for $k = 0.1$. The full line gives the $k \to 0$ limit of the LCS line, $z_t/l_T = 1 - 1/\nu$, which is equivalent to eq. (A.1). The dotted lines are calculated from the $p_s \to 0$ limit of (8.26) for $k = 0.1$ and various values of ϵ. For small p_s, these curves accurately describe the position of the tips of the ST branch of solutions given in (10.11). The solid circle at $\nu = 4.2$ and the solid square at $\nu = 8.7$ represent two data points of Esaka and Kurz [40], while the data points for $\nu = 1.3$ and $\nu = 4.2$ are obtained from ref. [25].

sponding to the LCS criterion, while the solid line gives the $k \to 0$ limit of the LCS result, obtained from a different argument by Bower et al. [28b]. See appendix A. The dotted lines show the ST matching prediction $z_t(p \to 0)$ for various values of ϵ as given in (10.13) above. The data point at $\nu = 4.2$ denotes a measurement by Esaka and Kurz [40] for cells at a Péclet number $p = \lambda V/2D$ of about 0.08, while those at smaller ν are measurements by Esaka [68] reported by Billia et al. [25]. These are the only measurements for cells that we can find in the literature [69]. The square symbol gives the tip velocity of the pattern that Esaka and Kurz [40] refer to as "dendritic cellular: some perturbations but no sidebranches". This plot illustrates quite clearly that the ST cellular shapes with narrow grooves are predicted to move up much less than what is apparently observed in experiments.

Although more experimental tests are obviously called for, we believe that the discrepancy between prediction and experiment uncovered in fig. 13 is real. Indeed, the finger-like cells that move up most and hence come closest to the data point(s), all have *wide* grooves and large wavelength, $\epsilon \to 1/2$ and $\lambda \to \infty$. For these very large wavelength solutions, a simple Mullins–Sekerka [1] type analysis [21] confirms in particular the LCS prediction that the $p \to 0$ ST branch is *unstable* for $\epsilon \to 1/2$, $\lambda \to \infty$.

We now briefly discuss various numerical results for two-dimensional models and compare them with the above predictions. As mentioned above, the two-dimensional one-sided model does appear to accurately describe the experiments of de Cheveigné et al. [8], but the values of σ given by the matching solutions are not consistent with those found for the narrow grooved cells that Misbah et al. [64] obtain numerically. Ramprasad et al. [70] have also studied the band of periodic cellular solution for parameter values relevant to de Cheveigné's experiments [8] at finite Péclet number. According to their calculations, the left edge of the band that corresponds to the minimum wavelength roughly coincides with the edge of the neutral stability band. Since the branch of solution we study unequivocally starts at wavelengths about a factor of 3 smaller, these authors apparently also investigate a different branch of solutions.

Kessler and Levine [35] also show several cellular profiles for parameter values $k = 0.16$, $p = 0.56$ relevant for de Cheveigné's experiments, but with a relatively large value of the diffusivity in the solid ($\beta \equiv D^s/D = 1/5$). Most of their cells have [71] a relative groove width ϵ of order 0.16–0.20. For the parameters in their fig. 1, we estimate $z_t/l_T \approx 0.61$ and $\nu \gtrsim 8$. Since the wavelength associated with this data point yields a value for σ as small as [72] 2×10^{-3}, we believe that the branch of solutions analyzed by Kessler and Levine [35] also is not the one which we analyze perturbatively. Note also that since the data point is well below the LCS line, this particular steady state solution may well be unstable.

In their extensive numerical simulations for $k = 0.4$, Ungar and Brown [4,73] observe various shapes with different values of ν and z_t/l_T. The cells in their [4] fig. 6a look rather realistic and have narrow grooves. We estimate that for these $\nu = 1.33$ and $z_t/l_T = 0.33$, whereas the matching prediction (10.13a) gives $z_t/l_T \approx 0.1$ for $\epsilon = 0.2$ and $z_t/l_T \approx 0.16$ for grooves as wide as $\epsilon = 0.4$ (the LCS prediction for this rather large value of k

is $z_t/l_T = 0.42$). We therefore believe that they are not members of the branch that we calculate. On the other hand, the cells in fig. 5c for $p = 0.4$ have wide grooves $\epsilon \approx 0.35$–0.4 and have $v = 5.7$ and $z_t/l_T = 0.49$. This tip position is indeed quite consistent with our matching estimate $z_t/l_T \approx 0.47$ for $\epsilon = 0.35$, but the wide grooved cells they show in this figure look rather unlike what one sees in typical experiments. They therefore support our conclusion that wide grooved cellular solutions do exist even at large p, but that these solutions are not the experimentally relevant ones. The more realistically looking cells in their figs. 10a and 10b ($v = 2.1$, $z_t/l_T = 0.43$, and $v = 3.2$, $z_t/l_T = 0.55$) are both significantly above the estimate (10.13a). It would therefore be interesting to investigate in more detail whether they are part of a different branch, as seems very likely.

In summary, our expansion method describes a branch of steady state solutions that is the extension to finite p (but k small) of the ST branch that has been analyzed [10,29,31] in detail for $p \to 0$. Since the grooves of these solutions with small σ are much wider than observed experimentally and in numerical work, and z_t is much smaller than the LCS value, we believe that this branch is not the physically relevant one, at least for Péclet numbers in the range (10.1). We propose the LCS criterion as a useful guide in studying both the stability of cells and the related "branch-selection" problem. Clearly, more experiments are called for, especially since wetting or surface preparation effects involving the cell thickness may be of important [6,8].

Finally, we wish to discuss the possible connection with other work on bifurcations and multiplicity of steady state cellular patterns. Our conclusions appear to be in line with those of Brener et al. [33]. These authors studied crystal growth in a channel, which corresponds to the $l_T \to \infty$ limit of DS. Not surprisingly, for small p, there is again a branch of Saffman–Taylor-like solutions. From the mapping to the ST problem, it follows that these solutions exist only for dimensionless undercoolings $\Delta > 1/2$, and that the velocity is a *decreasing* function of Δ. This is illustrated in fig. 14a. The decrease of V with increasing undercooling is, of course, counter-intuitive, and both analytical [74] and numerical [75] work indicate that the solutions in this branch are *unstable*. Note also that on this ST branch, the velocity V becomes arbitrarily large as $\Delta \to 1/2$. For fixed channel width, this means that finite Péclet number corrections to the shape will become more and more important as $\Delta \to 1/2$. Motivated by this observation, Brener et al. [33] argue that in the absence of surface tension anisotropy [76], the ST branch ends at a bifurcation point near $\Delta = 1/2$. See fig. 14b. Another "dendrite-like" branch bifurcates from this point as well, and it is this second branch of solutions that is believed to be stable [76].

Although the results of the simulations of Hunt [75] give some support for this scenario, we em-

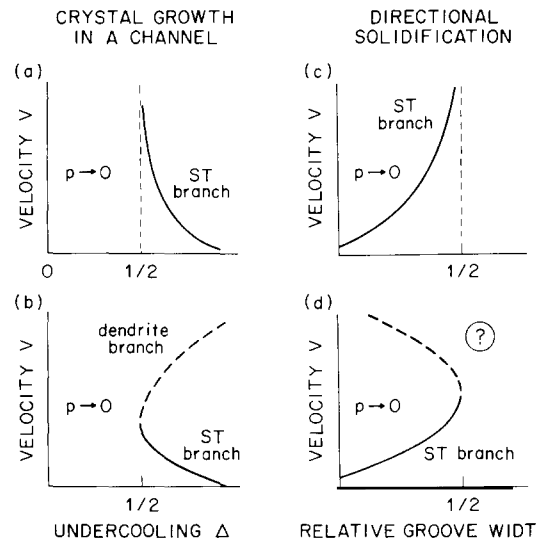

Fig. 14. (a), (b) Summary of the bifurcation structure for crystal growth in a channel as determined by Brener et al. [33]. (a) If the cellular profiles are modeled by the ST expression for the shape, one finds a ST branch for $\Delta > 1/2$. The velocity of these solutions diverges as $\Delta \to 1/2$. (b) Brener et al. [33] argue that if finite Péclet number corrections to the shape are taken into account, there is a bifurcation point for Δ close to $1/2$. From this point, both the ST branch and another "dendritic" branch bifurcate. Solutions on the ST branch are unstable, and those on the dendritic branch stable. (c), (d) Possible bifurcation diagram for directional solidification for small p, based on the analogous conjecture for crystal growth in a channel. (c) The velocity V diverges as the relative groove width approaches $1/2$. (d) In analogy with (b), it is possible that the ST branch merges with another cellular or dendrite branch near $\epsilon = 1/2$ and that solutions on the ST branch are unstable.

phasize that the analysis of Brener et al. [33] is non-rigorous in that it is based on a physically motivated but ad-hoc ansatz for the finite Péclet number corrections to the zero surface tension shape. At present, the arguments of Brener et al. [33] should therefore be considered somewhat speculative. The experimental situation is not completely clear either. Molho et al. [77] observe that there is a low-velocity small-Péclet number regime where the crystal shapes fit ST solutions very well and where the relative cell width $1 - \epsilon (= \Delta)$ is a decreasing function of V, as in fig. 14a. On the other hand, these shapes may be weakly unstable as expected theoretically [74,32]. Indeed, at higher growth rates a a crossover to a different high velocity regime is observed.

Returning now to the DS problem, numerical and analytical work has shown that multiple branches of solutions exist at finite Péclet numbers. We are not aware of any systematic study of the multiplicity of solutions in the limit $p \to 0$. However, the work of Brener et al. [33] illustrates that the behavior in this limit may be quite subtle.

Indeed, in analogy to crystal growth in a channel, let us consider the DS problem for a fixed set of experimental parameters. For *fixed wavelength*, the ST branch of solutions gives a relation between the growth velocity V and the relative groove width ϵ whose behavior is illustrated in fig. 14c. As in fig. 14a, the velocity diverges as $\epsilon \to 1/2$, where σ tends to zero. (For fixed λ, eq. (9.1b) shows that the vanishing of σ implies $V \to \infty$.) However, based on the similarity of crystal growth in a channel and the DS problem, we speculate that if the velocity dependence of the shape would be taken into account properly, one would likewise find that the ST branch merges with another cellular branch at a bifurcation point near $\epsilon = 1/2$ and that solutions on the ST branch are all unstable. Compare figs. 14b and 14d. The small ϵ solutions are almost certainly unstable since they lie outside the planar stability band, and both the analogy to crystal growth in a channel and our (LCS) stability argument suggest that all members of this branch are unstable (Karma and Pelce [31] argue that the ST branch is stable for an intermediate range of V). Note also that the postulated non-ST branch corresponds to much larger velocities at small ϵ than the ST branch. For fixed wavelength λ, (9.1b) shows that this conjectured branch is likely to have small groove width ϵ *and* small σ – precisely the characteristics that distinguish experimental cells form those on the ST branch! We hope that future analysis of the ideas of Brener et al. [33] will establish whether this scenario is correct.

There is another way to argue in favor of the existence of a bifurcation point analogous to the one predicted by Brener et al. [33]. Ungar and Brown [4,73] have also shown evidence for multipole solutions as a result of bifurcations with wavelength $\lambda/2$ off solutions with wavelength λ. This happens essentially when, upon increasing the velocity V, the tip region of wavelength λ undergoes a Mullins–Sekerka instability. For small p, our LCS criterion (and its refinements [21]) show precisely that the tips of the ST-like solutions will become Mullins–Sekerka unstable as $\epsilon \to 1/2$. Thus, according to Ungar and Brown [4,73], there is reason to expect the existence of a bifurcation point for ϵ close to $1/2$, which leads to an upper branch of higher velocity solutions analogous to fig. 14b.

Figs. 9 and 10 and the discussion of the finite amplitude cellular solutions in section 7 showed that at small ϵ our fingerlike patterns arise from matching grooves to cellular profiles that themselves are probably physically irrelevant, since they lie *outside* the planar instability band. Moreover, as is also clear from the mapping to the ST problem as $p \to 0$, they exist for *any* value of v above the threshold v_c, rather than a finite distance above threshold [78]. We believe that other possible branches of cells with grooves could be thought of as arising from joining up grooves to finite amplitude cells that lie within the planar instability band, even though the idea of a single matching region need not necessarily hold true. Evidence for the latter type of finite amplitude cells is given by the analytical work of Langer [1,51], Sivashinsky [16] and Kurtze [79] as well as by the numerical work of Ungar and Brown [4,73]. Note in this regard that in contrast to the solutions our matching method finds, the cellular profiles discussed by Sivashinsky [17] and Kurtze [79] for small k bifurcate off from the *center* of the

planer instability band (indicated by the square in fig. 3) and do *not* have a regular k expansion. Presumably some members of this latter finite amplitude branch of solutions develop deep grooves as ν is increased. Indeed, to our knowledge most numerical calculations [64,73,35] find deep cells by evolving continuously from small amplitude cells near the center of the planar instability band (near the square in fig. 3). These may correspond to the solutions indicated by the dashed line in fig. 14d.

If one accepts our conclusion that at least some of the numerical results are likely to correspond to solutions that are not on the extension of the ST branch to finite Péclet numbers, one may envision two different scenarios for how these various branches could be related:

(i) The ST branch is not connected to the experimental results and to the numerical results of refs. [4,35,65,73].

(ii) The ST branch is connected to the other branch(es) by some bifurcation(s).

Although there is at present insufficient information to convincingly decide between these two possibilities, the arguments of Brener et al. [33] for crystal growth in a channel as well as those of Ungar and Brown [4,73] make us favor the second scenario.

11. Final remarks

The main results and implications of our work for the existence and selection of cellular shapes with deep grooves are summarized at the end of section 1. We therefore confine ourselves here to drawing attention to a possible application of the LCS criterion to finite amplitude cells.

For materials for which diffusion in the solid is negligible the LCS criterion predicts that finite amplitude cells for fixed $\nu > 1$ are more likely to be found in experiments at Péclet number p of O(1) than at small p. The reason is that cell profiles for such materials have to obey the equal area rule (7.5b). As a result, the dimensional value of z_t of finite amplitude cells has to be of order $\lambda/2$, so that for these $\zeta_t \approx (\nu - 1) - (1 - k)p$. Therefore, finite amplitude cells can only obey the LCS criterion $\zeta_t \approx 0$ for $(\nu - 1)/(1 - k) \approx p$. For larger values of ν, we expect finite amplitude cells to be unstable. Thus, we predict that the relative velocity range in which stable finite amplitude cells can be observed scales with the Péclet number p. Although we are not aware of any systematic study of this question, these predictions are consistent with the fact that Trivedi [5] reports finite amplitude cells only very close to threshold for $p \approx 0.02$, whereas de Cheveigné et al. [6] have seen finite amplitude cells with $p \approx 0.25$ at $V/V_c \approx 1.4$ (i.e., $\nu - 1 \approx 0.4$). We hope that these observations will be extended so that the above suggestion can be tested systematically.

Appendix A. Other approaches

Bower, Brody and Flemings [28b] (BBF) arrived at an equation similar to the LCS criterion using matching arguments similar in spirit to those found in section 8. Ignoring curvature corrections, they used the approximation $(\partial u/\partial z)_i \approx \mathrm{d}u_L/\mathrm{d}z = -1/l_T$ (see (2.20)) to estimate the gradient $(\partial u/\partial z)_t$ at the tip. (We use dimensional lengths as in section 2.) While eq. (6.2) shows that $(\partial u/\partial z)_i \approx -1/l_T$ is a very accurate approximation in the grooves, there may be notable corrections near the tip. (Indeed, $(\partial u/\partial z)_t$ is given exactly by the boundary condition (2.16). It is only when $\zeta_t = 0$ that the two expressions are equal.) Then, treating the pattern tips as planar, in essence BBF approximated the field in front by $u \approx u_t\, \mathrm{e}^{-(z-z_t)/l_D}$, and matched the gradient at the tip $(\partial u/\partial z)_t$ calculated from this "far field" result to the liquidus gradient calculated above. This gives $-u_t/l_D = -1/l_T$ or

$$\nu u_t^{\mathrm{BBF}} = 1. \tag{A.1}$$

See eq. (17) in appendix A of ref. [28b]. Hunt and coworkers [22,23,27] developed this approach further and tried to estimate corrections due to interface curvature. We note that (A.1) is equivalent to the $k = 0$ limit of the LCS criterion, though the ideas leading to the two results are rather different. While there are several points that might be criticized in the above argument, and the connections to a stability analysis are obscured, eq. (A.1)

does have the virtue that u_t^{BBF} is always greater than zero, in contrast to the LCS criterion for $v > 1/k$. (The value of z_t predicted by (A.1) is always less than that given by the LCS condition $\zeta_t = 0$, which we have argued [21] is an *upper bound* to the distance tips have to move to achieve stability. See also appendix D.) Indeed (A.1) appears to be a useful first approximation even in the dendritic regime, and most later attempts to provide a more detailed treatment have proven less successful [13]. (See, however, ref. [80] for a modern treatment of stability in the dendritic regime.)

Based on arguments such as these, the idea that constitutional supercooling should be small near the tips of experimental patterns was stated explicitly in the early literature. See, e.g., ref. [2], p. 84, and ref. [81]. However, it was not emphasized that it is primarily through changes in z_t rather than changes in cell spacing or curvature that this condition can be approximately satisfied in the cellular regime. Moreover, attempts to apply these ideas outside their limited regime of validity (e.g., to materials with large k and/or large $v > 1/k$) led to criticism of the basic concept (see, e.g., refs. [81] and [82]), and these ideas are not discussed in most current treatments. Very recently, however, Billia and coworkers [13,25] have stressed the empirical fact that relations like (A.1) hold approximately for many experimental patterns, and independently of us, have pointed out that this seems to disagree with the values of ζ_t given by the matching to Saffman–Taylor fingers [83].

Appendix B. Conservation equations allowing for diffusion in the solid

If $\beta \equiv D^s/D$ is non-zero, then the term $\beta(\hat{n} \cdot \nabla u)_i^s$ should be added to the right-hand side of the conservation equation (4.5) to take account of the diffusion flux into the solid. The result can be written

$$p_s \, \Delta u_i \cos\theta = -\left[\left(\frac{\partial u}{\partial z}\right)_i - \beta\left(\frac{\partial u}{\partial z}\right)_i^s\right]\cos\theta + \left[\left(\frac{\partial u}{\partial x}\right)_i - \beta\left(\frac{\partial u}{\partial x}\right)_i^s\right]\sin\theta, \tag{B.1}$$

where we note that $\hat{n} = \cos\theta\hat{z} - \sin\theta\hat{x}$. Eq. (B.1) allows us to determine corrections for non-zero β to the results (7.2) and (5.4), which hold for $\beta = 0$.

In particular, eq. (5.4) follows from (B.1) by setting $\beta = 0$, and dividing by $\sin\theta$. The term $(\partial u/\partial x)_i$ in (B.1) can be exactly re-expressed as

$$\left(\frac{\partial u}{\partial x}\right)_i = \int_0^{x_i} \mathrm{d}x \frac{\partial^2 u}{\partial x^2} = -\int_0^{x_i} \mathrm{d}x \left(\frac{\partial^2 u}{\partial z^2} + p_s \frac{\partial u}{\partial z}\right), \tag{B.2}$$

noting that $\partial u/\partial x$ vanishes by symmetry at $x = 0$, and using the diffusion equation (4.4). Substituting (B.2) into (B.1) with $\beta = 0$ yields eq. (5.4).

The inner equation (6.4), which describes the deep grooves and the matching region in the limit $\beta = 0$, follows from (5.4) on approximating the integrals in (B.2) as

$$\left(\frac{\partial u}{\partial x}\right)_i \approx -x_i\left(\frac{\mathrm{d}^2 u_i}{\mathrm{d}z^2} + p_s \frac{\mathrm{d}u_i}{\mathrm{d}z}\right), \tag{B.3}$$

using the steepness and narrowness of the grooves, as discussed in section 6. Note that the first term on the right in (B.3) is most important in the matching region, as shown in section 9, while deep in the grooves the second term dominates, leading to the linear term in the Scheil equation (6.6).

These considerations lead to a criterion predicting when the results of the one-sided model, and in particular, the Scheil equation describing deep grooves, must be significantly modified for $0 < \beta \ll 1$. Deep in the grooves where the curvature is very small the dominant effect of the added terms in (B.1) is to replace the Scheil equation (6.6) by

$$\zeta \, \mathrm{d}x_i/\mathrm{d}z = p_s x_i - \beta(v/p_s)(\partial u/\partial x)_i^s. \tag{B.4}$$

For small β, it is reasonable to ignore the last term on the right hand side of (B.4) until it is of the same order of magnitude as the first. Thus the Scheil equation can be trusted until we get to sufficiently large values of $-z$ that

$$\zeta \, \mathrm{d}x_i/\mathrm{d}z \approx \beta(v/p_s)\left|(\partial u/\partial x)_i^s\right|, \tag{B.5}$$

or, equivalently from eq. (B.1), until $(\partial u/\partial x)_i \approx \beta\,|(\partial u/\partial x)_i^s|$. Using eq. (C.1) to evaluate $(\partial u/\partial x)_i^s$, an accurate approximation until about the breakdown distance ζ_b, and the lowest order

estimate $(\partial u/\partial z)_i = \mathrm{d}u_i/\mathrm{d}z = -p_s/v$ yields the criterion

$$\zeta_b \cot^2\theta_b \approx \beta k. \tag{B.6}$$

For very small β, the grooves can be nearly vertical before the assumptions of the one-sided model and the Scheil equation must break down. Note that the initial effect of the added term is to produce a more rapid closing of the grooves, as is clear on physical grounds.

Appendix C. Effect of diffusion in the solid

In section 5, we gave a systematic and rather general treatment of the shape of the narrow grooves between fingers. The main limitation was our use of the one-sided model, where $\beta = D^s/D = 0$. Deep in the grooves where curvature corrections become negligible our results reduce to those of the classical Scheil equation, which predicts infinitely deep grooves with power law shapes.

However, experiments as well as numerical solutions of the DS equations with $\beta > 0$ find grooves with large but *finite* depth, often terminated by a bubble-like closure. Actually, it is easy to show that the predictions of the Scheil equation must eventually break down sufficiently deep in the grooves for any nonzero β, no matter how small. The main physical effect can be seen from fig. 1b, which shows numerical solutions of the DS equations with β small but non-zero [4]. We see that for steep grooves, very large gradients build up in the solid near the interface. Indeed, the existence of such large gradients is predicted by he one-sided model. Using eq. (2.19) we have

$$\left(\frac{\partial u}{\partial x}\right)_i^s = k\left(\frac{\partial u}{\partial x}\right)_i + k\left(\frac{\partial u}{\partial z}\right)_i \frac{\mathrm{d}z_i}{\mathrm{d}x}. \tag{C.1}$$

The Scheil equation (6.6) predicts that $\mathrm{d}z_i/\mathrm{d}x = \tan\theta$ becomes arbitrarily large deep in the grooves for sufficiently large $\zeta \equiv (v-1) - (1-k)p_s z$, implying arbitrarily large values of $(\partial u/\partial x)_i^s$. On the other hand, if $\beta > 0$, then these large gradients must eventually produce an appreciable diffusion flux proportional to $\beta(\partial u/\partial x)_i^s$ in the solid, thus leading to a breakdown of the one-sided model, and of the Scheil shapes derived using it.

Based on this idea, a quantitative estimate of the breakdown distance ζ_b is carried out in appendix B, where the effects of non-zero β are taken into account. We find that the predictions of the Scheil equation must be appreciably modified by the effects of diffusion in the solid when

$$\zeta_b \cot^2\theta_b \approx \beta k. \tag{C.2}$$

For sufficiently small β, it is only very far from the tip region that diffusion in the solid must induce a breakdown of the groove shapes predicted by the one-sided model.

This criterion is to be contrasted with that given by Kessler and Levine [34]. They argue that there exists a minimum groove width $x_{\min} \propto k$, or equivalently, a lower bound to the cell depth of order k^{1-k}, *independent* of the value of β. However, their estimate is based on the assumption that the impurity distribution in the solid near the groove closing has a simple quadratic dependence on x, rather than the very inhomogeneous distributions seen in fig. 1b.

In principle, theirs is the correct limiting distribution an infinite distance from the tip, where the initial inhomogeneous impurity distribution in the solid, estimated as in eq. (B.1), has had time to re-equilibrate by lateral diffusion. However, since the typical impurity in the solid must diffuse a distance of order the cell width during this equilibration process, a (dimensional) time of order $\tau_{eq} \propto \lambda^2/D^s$ is required. For impurities initially captured near the tip, this occurs at a distance Δz from the tip of order $\Delta z \approx V\tau_{eq} = 2p\lambda/\beta$. Thus β is implicitly involved in the Kessler and Levine [34] treatment, since only sufficiently far from the tip (a distance proportional to β^{-1}) can the equilibration assumption hold true.

In practice, for most solidification cells with small β, equilibration in the solid is almost never achieved, particularly if the (large) temperature dependence of D^s is also taken into account. Thus the treatment we have given based on the *initial* breakdown of the inhomogeneous solid impurity distribution as given by the one-sided model seems more physically relevant for cells with small β.

Our treatment of the groove corrections caused by diffusion in the solid illustrates several points we believe should be considered in assessing the utility of the one-sided model. In contrast to the impression the casual reader might get from ref. [34], we argue that the one-sided limit offers a simple and generally useful starting point to describe many features of patterns seen in systems with β small but non-zero.

Certainly the one-sided model can never (except for the unphysical case $k \equiv 0$) reproduce a final equilibrated solid distribution with $u^s = 0$ independent of x, which in principle is the correct boundary condition to impose in the solid far from the interface as $z \to -\infty$. In practice, however, for β small there is often an "intermediate asymptotic" regime [84] extending far behind the tip region where almost no solid state diffusion has taken place. This is the regime found in most experiments. Thus the lack of equilibration in the solid can often be taken as a strength, rather than a weakness of the one-sided model.

Further, the accuracy of the patterns predicted using the one-sided model depends on the *shape* of the patterns. As we have seen in eq. (C.2), if the grooves become too steep, corrections to the one-sided model must become important. A related but more obvious limitation occurs in the description of the "melting" portion of reentrant patterns, where the interface position z_i is not a single-valued function of x. Above such "melting" interfaces, a thin boundary layer will form, whose thickness is proportional to β, such that $\beta(n \cdot \nabla u)_i^s$ does not vanish as $\beta \to 0^+$. The description of these boundary layers and of the reentrant portion of the interface cannot be consistently carried out in the one-sided limit where $\beta(n \cdot \nabla u)_i^s$ is assumed to vanish [34].

However, most experimental finite amplitude or fingerlike cell patterns are either single-valued, where such boundary layers do not form, or have only a small reentrant portion, as in the upper part of a bubble closure. For these patterns the one-sided model offers a physically relevant and computationally very useful starting point, particularly for analytic work. In ref. [26], we gave a simple approximate treatment of the bubble closures found for two-dimensional patterns, based on conservation requirements and the idea that the boundary layer region above the reentrant part of the bubble, where the one-sided impurity distribution fails, is very small. We will not repeat the analysis here, since it is somewhat technical, and still not applicable to real three-dimensional patterns, where the closures undergo an instability similar to that seen for a dripping faucet [85].

However, we mention that the location of the closure in two dimensions seems not to be related to the breakdown distance calculated in eq. (C.2). Instead it depends mainly on k and the matching parameter ϵ, and is essentially independent of β.

Appendix D. Constitutional supercooling near an arbitrary point on the interface

In general, let $\boldsymbol{r}_i \equiv (x_i(z), z)$ denote an arbitrary point on the interface of a fingerlike pattern, and $\boldsymbol{r}_\alpha \equiv \boldsymbol{r}_i + \alpha l_T \hat{n}$ a point in the adjacent fluid layer for a small normal displacement of magnitude αl_T with $\alpha \ll 1$. (We use dimensional lengths as in section 2.) Neglecting curvature corrections, a measure of the net supercooling at $\boldsymbol{r}_\alpha$ is $u_L(\boldsymbol{r}_\alpha) - u(\boldsymbol{r}_\alpha)$, where $u_L(\boldsymbol{r}_\alpha) = u_L(z_\alpha)$ is given by (2.20). Of course, this difference vanishes as $\alpha \to 0$, and a more relevant measure is the *differential supercooling*

$$\delta u_\alpha^{LCS} \equiv \left[u_L(\boldsymbol{r}_\alpha) - u(\boldsymbol{r}_\alpha) \right] / \alpha. \tag{D.1}$$

If δu_α^{LCS} is positive, then the fluid at an infinitesimal distance normal to the interface is constitutionally supercooled. Expanding both $u_L(\boldsymbol{r}_\alpha)$ and $u(\boldsymbol{r}_\alpha)$ in a Taylor series about $\alpha = 0$ and using (2.15)–(2.20) yields

$$\delta u_\alpha^{LCS} = (\nu \Delta u_i - 1) \cos\theta \approx \zeta(z) \cos\theta, \tag{D.2}$$

where $\zeta(z)$ is (3.4) evaluated at the general position z. Although ζ becomes large deep in the grooves, we can use the Scheil results (6.6) and (6.7) to give for large ζ

$$\delta u_\alpha^{LCS} = \sin\theta \; x_i / l_D. \tag{D.3}$$

This indeed vanishes for large ζ from (6.7). Thus we can show explicitly that the differential supercooling is very small (but positive) in the grooves,

because of the cos θ factor in (D.2). This is true for any pattern that has deep grooves, and does not distinguish between different members of a family of solutions. However, if we require that $\delta u_\alpha^{\mathrm{LCS}}$ is small near the tip, where the estimate (D.3) is inaccurate, we arrive at the LCS criterion from (D.2). In general $\delta u_\alpha^{\mathrm{LCS}}$ is very small but positive in the grooves, and we expect it will remain small but positive near the tips of experimentally selected patterns. This is consistent with the results of ref. [21], which showed that the corrections to (3.4) all tend to increase (slightly in the cellular regime) the value of ζ_t.

Appendix E. Derivation of eqs. (7.13)–(7.16)

Since (7.10)–(7.12) satisfy the diffusion equation (4.4), the remaining equations to be solved by the coefficients B_n are the interface condition (4.6) and the flux conservation boundary condition (4.5). Writing the latter condition in the form (B.1) with $\beta = 0$ and noting that $\tan\theta = \mathrm{d}z_i/\mathrm{d}x$, we obtain upon substitution of (7.10) the equations

$$k\,\mathrm{e}^{p_0(z_i - z_m)} - kB_0 - \sum_{n\geq 1} B_n\left(\frac{p_n - p_0}{-p_0} + k\right) \times \mathrm{e}^{-(p_n - p_0)(z_i - z_m)}\cos(q_n x) = -\frac{1}{p_0}\sum_{n\geq 1} B_n\,\mathrm{e}^{-(p_n - p_0)(z_i - z_m)}\,q_n\sin(q_n x)\frac{\mathrm{d}z_i}{\mathrm{d}x}. \tag{E.1}$$

Upon multiplication of this result by the factor $\exp[-p_j(z_i - z_m)]\cos(q_j x)$ and integration over x, we obtain a set of equations of the form (7.13) with N_j given by (7.14) and M_{jn} given by

$$M_{jn} = \int_0^a \mathrm{d}x\,\cos(q_j x)\cos(q_n x) \times \mathrm{e}^{-(p_j + p_n - p_0)(z_i - z_m)}\left(\frac{p_n - p_0}{p_0} + k\right) + \int_0^a \mathrm{d}x\,\cos(q_j x)\,q_n\sin(q_n x) \times \frac{\frac{\mathrm{d}}{\mathrm{d}x}\left(\mathrm{e}^{-(p_n + p_j - p_0)(z_i - z_m)}\right)}{p_0(p_n + p_j - p_0)}. \tag{E.2}$$

After a partial integration, the second term on the right-hand side becomes

$$-\int_0^a \mathrm{d}x\left[q_n^2\cos(q_j x)\cos(q_n x) - q_n q_j\sin(q_n x)\sin(q_j x)\right] \frac{\mathrm{e}^{-(p_n + p_j - p_0)(z_i - z_m)}}{p_0(p_n + p_j - p_0)}. \tag{E.3}$$

Upon combining this with the first term in (E.2) using the fact that according to (7.12) $q_n^2 = p_n(p_n - p_0)$, we then obtain eq. (7.15) for the M_{jn}.

Note that (7.13) for $j = 0$ takes the form

$$\sum_{n\geq 0} M_{0n}B_n = N_0. \tag{E.4}$$

Since

$$M_{0n} = k\int_0^a \mathrm{d}x\,\cos(q_n x)\exp\left[-p_n(z_i - z_m)\right],$$

and $N_0 = ka$, this becomes in view of (7.10)

$$k\int_0^a \mathrm{d}x\left[u(x, z_i) - 1\right] = 0, \tag{E.5}$$

which is the conservation condition (5.3) evaluated in the solid from which the equal area rule (7.5) was derived.

References

[1] J.S. Langer, Rev. Mod. Phys. 52 (1980) 1.

[2] M.C. Flemings, Solidification Processing (McGraw-Hill, New York, 1974).

[3] W. Kurz and D.J. Fisher, Fundamentals of Solidification (TransTech, Switzerland, 1984).

[4] L.H. Ungar and R.A. Brown, Phys. Rev. B31 (1985) 5931; B29 (1984) 1367.

[5] R. Trivedi, Met. Trans. 15A (1984) 977.

[6] S. de Cheveigné et al., unpublished.

[7] P.E. Cladis, J.T. Gleeson and P.L. Finn, in: Nonlinear Evolution of Spatio-Temporal Structures in Continuous Systems, Eds. F.H. Busse and L. Kramer (Plenum, New York, 1990).

[8] S. de Cheveigné, C. Guthmann and M. Lebrun, J. Physique 47 (1986) 2095.

[9] See, e.g., also M.A. Eshelman and R. Trivedi, Acta Met. 35 (1987) 2443.

[10] T. Dombre and V. Hakim, Phys. Rev. A36 (1987) 2811; see also M. Ben-Amar, T. Dombre and V. Hakim, in:

Propagation in Systems Far from Equilibrium, Eds. J.E. Wesfreid et al. (Springer, Berlin, 1988) p. 35.
[11] See, e.g., D. Bensimon, L.P. Kadanoff, S. Liang, B.I. Shraiman and C. Tang, Rev. Mod. Phys. 58 (1986) 977.
[12] P. Pelcé and A. Pumir, J. Crystal Growth 73 (1985) 337.
[13] B. Billia, H. Jamgotchian and L. Capella, J. Crystal Growth 82 (1987) 747; 94 (1989) 987.
[14] See, e.g., P.C. Hohenberg and M.C. Cross, in: Fluctuations and Stochastic Phenomena in Condensed Matter, Ed. E. Garrido (Springer, Berlin, 1987).
[15] Near a point where the bifurcation crosses over to subcritical, the stable solutions can actually lie outside the planar instability band. See W. Eckhaus and G. Iooss, Physica D39 (1989) 124, for a detailed discussion of this point.
[16] G.I. Sivashinsky, Physica 8D (1983) 243;
see also D. Wollkind and L. Segel, Phil. Trans. Roy. Soc. London 268 (1970) 351.
[17] See, e.g., P. Haug, Phys. Rev. A40 (1989) 7253, and references therein.
[18] See fig. 2 of M.J. Bennett, R.A. Brown and L.H. Ungar, in: Physics of Structure Formation, Eds. W. Güttinger and G. Dangelmayr (Springer, Berlin, 1987), for an example of the variation of the planar instability band with k.
[19] J. Bechhoefer, A.J. Simon, A. Libchaber and P. Oswald, Phys. Rev. A40 (1989) 2042.
[20] K. Brattkus and C. Misbah, Phys. Rev. Letters 64 (1990) 1935.
[21] J.D. Weeks and W. van Saarloos, Phys. Rev. A42 (1990) 5056.
[22] See, e.g., D.J. Allen and J.D. Hunt, Met. Trans. 7A (1976) 767.
[23] M.H. Burden and J.D. Hunt, J. Crystal Growth 22 (1974) 99, 109.
[24] W. Kurz and D.J. Fisher, Acta Met. 29 (1981) 11.
[25] B. Billia, H. Jamgotchian and R. Trivedi, unpublished. These authors attribute the idea that the constitutional supercooling at the tip is small to H.D. Brody and M.C. Flemings [28]. See also appendix A.
[26] J.D. Weeks and W. van Saarloos, Phys. Rev, A39 (1989) 2772. The definition for ζ in this reference differs by a factor $(\nu - 1)$ from that used in the present paper and ref. [21].
[27] See J. Hunt, in: Solidification and Casting of Metals (Metals Society, London, 1979).
[28] (a) H.D. Brody and M.C. Flemings, Trans. Met. Soc. AIME 236 (1966) 615;
(b) T.F. Bower, H.D. Brody and M.C. Flemings, Trans. Met. Soc. AIME 236 (1966) 624.
[29] M. Mashaal, M. Ben-Amar and V. Hakim, Phys. Rev. A41 (1990) 4421.
[30] See, e.g., M. Van Dyke, Perturbation Methods in Fluid Mechanics (Parabolic, Stanford, CA, 1975), for an introduction to matched asymptotic expansions.
[31] A. Karma and P. Pelcé, Phys. Rev. A39 (1989) 4162; Europhys. Letters 9 (1989) 713;
see also A. Karma and P. Pelcé, Phys. Rev. 41 (1990) 6741.
[32] See, e.g., D.A. Kessler and H. Levine, Mod. Phys. Letters B2 (1988) 945, and references therein.
[33] E.A. Brener, M. Geilikman and D.E. Temkin, Zh. Eksperim. Teor. Fiz. 94 (1988) 241 [Soviet Phys.-JETP 67 (1988) 565].
[34] D.A. Kessler and H. Levine, Phys. Rev. A39 (1989) 3041.
[35] D.A. Kessler and H. Levine, Phys. Rev. A39 (1989) 3208.
[36] Note that we take m_L positive; in some papers, m_L is taken negative.
[37] See, e.g., D. Kessler and H. Levine, Acta Met. 36 (1988) 2693.
[38] There is no standard notation in this field. We follow Langer [1] in our definitions for l_T and d_0, as well as for the dimensionless control parameter ν introduced in eq. (3.2). Many workers define the diffusion length as $l \equiv 2D/V = 2l_D$ and some write c_0 for our c_∞ or our c_t, where c_t is the concentration at the tip of a pattern. Others have definitions for ν and the Péclet number p, defined in eq. (4.2), that differ from ours by factors of 2. These notational differences have caused some confusion in the literature.
[39] Recently, D.A. Kessler and H. Levine, Phys. Rev. A41 (1990) 3197 have investigated whether an array of cells could show a zero wavenumber oscillatory instability, so that above the threshold for instability all cells would oscillate in phase. The possibility of such an instability had been suggested by A. Karma and P. Pelcé in ref. [31]. No evidence for such an instability was found by Kessler and Levine. However, they used the symmetric model. Note in this regard that the predictions of ref. [31] were for the one-sided model.
[40] H. Esaka and W. Kurz, J. Crystal Growth 72 (1985) 578.
[41] Eq. (4.3) is accurate for small k or if the Péclet number p defined in (4.2) is small. See, e.g., refs. [1] and [21].
[42] This can be shown by an analysis similar to the one given by Dombre and Hakim [10].
[43] See, e.g., fig. 1b of ref. [26].
[44] In an earlier account of this work [26], we used a slightly different empirical expression for the outer diffusion field. This expression reduces to (7.1) in the limit $k \to 0$ and was motivated by the fact that the boundary condition (4.5) can be exactly rewritten in the form $[u_i + p_s^{-1}\, \mathrm{d}u_i/\mathrm{d}z - k(u_i - 1)] = p_s^{-1}(\partial u/\partial x)_i/\sin\theta\cos\theta$. If one neglects the right hand side on the basis that the profiles of Ungar and Brown shown in fig. 1 are very one-dimensional, even though $k = 0.4$, an integration of the left-hand side yields eq. (8) of ref. [26]. In addition to the fact that this expression is rather ad hoc, it also does not resolve the problem that realistic solutions with relatively small curvatures lying within the planar instability band seem to exist only by virtue of the deviations from a one dimensional profile.
[45] Eq. (7.3) can easily be generalized to the case of fourfold anisotropy with the capillary length given by (2.4). For finite amplitude cells, the equal area rule (7.5) remains valid with fourfold anisotropy.
[46] Numerical solutions to eqs. (7.6)–(7.9) that have to satisfy

the constraint (7.5) are easy to obtain using standard shooting programs. We used a routine based on the program SHOOT of Numerical Recipes by W.H. Press et al. (Cambridge University Press, Cambridge, 1986). Solutions like those shown in fig. 6 can be found in real time on a small computer.

[47] Note that a virtue of our choice of a length scale independent of pattern wavelength is that we can solve (7.5)–(7.9) as a simple initial value problem whose degrees of freedom are clearly seen. The dimensionless half wavelength a can be directly computed for a given set of experimental parameters. The alternative choice of $\lambda/2$ as unit of length gives the additional boundary condition $x=1$ at the tip. Of course the final results are independent of the particular choice, but conceptually the present choice has the advantage that the parameters that are controlled in an experiment remain fixed.

[48] This is actually easy to check explicitly in the small amplitude limit. In this limit, the impurity profile in the liquid has just one nontrivial mode, q_1 (see, e.g., ref. [1]). It is then straightforward to check from eqs. (7.13)–(7.15) that B_1 is indeed linear in the amplitude and in k in this limit.

[49] For fixed parameters B_j, the profile can be integrated as in eqs. (7.6)–(7.9); at the same time, the matrix elements M_{jm} and N_j can be obtained by introducing new variables as in (7.9). The conditions (7.13) are then imposed as boundary conditions at the tip, and solutions are obtained by the standard shooting program.

[50] As stated before, in the small amplitude limit the wavelength of the cellular solutions considered here should approach the neutral stability wavelength λ_s whose $k \to 0^+$ limit λ_s^0 is given in eq. (4.3). We have checked that the variation of λ_s with k apparent in fig. 9 agrees with the linear stability analysis of the one-sided model given in ref. [1].

[51] J.S. Langer, Acta Met. 25 (1977) 1121; see also ref. [1].

[52] B. Caroli, C. Caroli and B. Roulet, J. Physique 43 (1982) 1767.

[53] G.J. Merchant and S.H. Davis, Phys. Rev. Letters 63 (1989) 573.

[54] In the viscous fingering literature, $1-\lambda$ is conventionally used to denote the groove width, rather than ϵ; refs. [10], [29] and [31] follow this convention. We prefer to reserve λ for the wavelength of the pattern, however.

[55] As mentioned in footnote 11 of ref. [26], the original estimate given by Dombre and Hakim [10] differed from this value, but the value given here is now generally accepted to be correct.

[56] See also the discussion of Dombre and Hakim [10]. We have extended the analysis to show that in the next order, the matching conditions actually prescribe $\beta=0$.

[57] In practice, we first fix the product ϵa in (8.18), and then integrate up to the tip to obtain a. From the known value of a, we then get the corresponding value of ϵ.

[58] In ref. [29], the term analyzed in eqs. (8.22) and (8.23) is replaced by the area in the grooves. One can check that the right-hand side of our (8.23) equals their integral I_2, defined after (II.8). Our eq. (8.26) reduces to the second equation after (II.8) of ref. [29] when the Péclet number p is small enough that the second term between square brackets in (8.26) can be neglected. Beware of notational differences between our paper and ref. [29]. The authors of ref. [29] use 2ν where we use ν, a Péclet number $P=2p$, and their grooves point in the positive x direction.

[59] Even if infinitely deep grooves could exist, they are not correctly given by eq. (6.4) because of the breakdown of the one-sided model. See appendices B and C.

[60] Note that σ as defined here has a well-defined limit both as $p \to 0$ and as $\nu \to \infty$. In the latter case it reduces to the standard stability parameter for dendritic growth [1] if we replace $\lambda/2$ by the tip radius. Mashaal et al. [29] define a different $\sigma^{\mathrm{MBH}} = (\nu-1)\sigma/4$; Dombre and Hakim [10] (after some misprints have been corrected; see footnote 11 of ref. [26]) use $\sigma^{\mathrm{DH}} = \sigma/4$, while Karma and Pelcé [31] use the quantity $C^{\mathrm{KP}} = 4\zeta_t/[\nu-1)\sigma]$. The factor 4 arises in these transcriptions because the wavelength λ rather than the half-wavelength $\lambda/2$, is taken as the unit of length.

Although this is not the usual practice, we believe it would be useful in general to define σ as a measure of the appropriate neutral stability length λ_s relative to the pattern scale ($\lambda/2$ for cells, the tip radius of curvature for dendrites). If we use this definition, it turns out that the selected value of σ for dendrites in the one-sided model and the two-sided model are roughly the same. (The usual definition for σ does not take account of the fact that the neutral stability lengths differ [1] in these two cases, and the resulting σ values then differ by a factor of 2.) See Y. Saito, G. Goldbeck-Wood and H. Müller-Krumbhaar, Phys. Rev. A38 (1988) 2148 and C. Misbah, J. Physique 48 (1987) 1265.

[61] Note that a different definition of d_0 is used in ref. [8] and that there are some misprints in this paper as well. For a comparison with eq. (2.19), c_0 in the definition of d_0 following eq. (4) in this reference should be replaced by c_∞. With the values in the table of this paper, we then obtain $d_0 = 4.3\times10^{-6}$ cm. Using $D=1.2$ cm^2/s and $\lambda^2 V \approx 3.2\times10^{-8}$ cm^3/s for the data shown in fig. 2, we obtain the value in eq. (10.1) for σ as defined in (9.1). We thank S. de Cheveigné for helpful correspondence concerning the proper values of these parameters.

[62] Note also that in ref. [8] the comparison with Karma's results [Phys. Rev. Letters 57 (1986) 858] is incorrect. It is now generally agreed that Karma's code effectively determined the zero groove width solution ($\epsilon=0$, $\sigma=\sigma_{\max}$). In our notation, the value of $\sigma_{\max}$ Karma determined is of order unity and agrees with the small p results of ref. [10] and this work.

[63] P. Kurowski, Thesis, Université Paris VII (1990), unpublished.

[64] C. Misbah, H. Müller-Krumbhaar and Y. Saito, unpublished.

[65] Our σ^{ST} is equal to d_0/π^2 in the notation of ref. [10], $4/C$ in eq. (22) of the first paper in ref. [31], and $4\sigma_{ST}$ as defined in ref. [29].
[66] V. Seetharaman, M.A. Eshelman and R. Trivedi, Acta Met. 36 (1988) 1175.
[67] M. Ben-Amar and B. Moussallam, Phys. Rev. Letters 60 (1988) 317.
[68] H. Esaka, Thesis, Ecole Polytechnique de Lausanne (1986), unpublished.
[69] Although measurements of the tip temperature (and hence z_t/l_T) in the cellular regime are scarce, there are several such measurements in the dendritic regime. See, e.g., refs. [23] and [24].
[70] N. Ramprasad, T.C. Lee and R.A. Brown, unpublished.
[71] We estimate this from fig. 2 of ref. [35].
[72] Kessler and Levine [35] also use different definitions for d_0 and σ. They define $d_0^{KL} = d_0(1-k)/k$ and $\sigma^{KL} = (\nu - 1)\sigma/(2k\nu)$. Note that the σ value of the solution studied in ref. [35] is a factor of 3 smaller than the value given in (10.1) for the experimental patterns. This difference was not noted in ref. [35] because of the incorrect value of σ given in ref. [8]. See ref. [61].
[73] L.H. Ungar and R.A. Brown, Phys. Rev. B29 (1984) 1367; B30 (1984) 3993;
L.H. Ungar, M.J. Bennett and R.A. Brown, Phys. Rev. B31 (1985) 5923.
[74] P. Pelcé, Europhys. Letters 7 (1988) 453.
[75] J.D. Hunt, unpublished.
[76] In ref. [21], we incorrectly state that this bifurcation structure is only found if interface kinetics is taken into account. It is the velocity dependence of the shape correction, not the interface kinetics, that is important for the existence of a second branch. We are grateful to the referee for pointing this out to us.
[77] P. Molho, A.J. Simon and A. Libchaber, Phys. Rev. A42 (1990) 904.
[78] As (10.10) illustrates, a factor $\nu - 1$ arises in the mapping to the ST problem. This appear to suggest that these cellular solutions exist for any $\nu > 1$. However, this factor is equal to $\nu - \nu_c$ to lowest order in p since $\nu_c = 1 + O(p^{1/3})$ (see, e.g., ref. [1]). In our matching analysis, the fact that these solutions exist for any $\nu > \nu_c$ can be seen quite naturally from the fact that there is always a branch of finite amplitude solutions outside the planar instability band for any $\nu > \nu_c$. Compare fig. 9.
[79] D.A. Kurtze, Phys. Rev. B37 (1988) 370.
[80] J.A. Warren and J.S. Langer, Phys. Rev. A42 (1990) 3518.
[81] R.M. Sharp and A. Hellawell, J. Crystal Growth 6 (1970) 253.
[82] W.A. Tiller, Can. J. Phys. 37 (1959) 1204.
[83] M. Hennenberg and B. Billia, unpublished. We are grateful to B. Billia for giving us a preprint of this paper.
[84] G.I. Barenblatt, Similarity, Self-Similarity, and Intermediate Asymptotics (Plenum, New York, 1980).
[85] K. Brattkus, J. Physique 50 (1989) 2999.